minerals

MDPI

Article

U-Pb Geochronology of Fersmite: Potential Time Constraints on Magnesite Formation, Sparry Dolomitisation, and MVT Pb-Zn Mineralisation in SE British Columbia, Canada

Matthew I. Leybourne [1,2,*], George J. Simandl [3], Joseph A. Petrus [4], Suzanne Paradis [5], Carlee Akam [6], Alexander Voinot [7], Douglas Archibald [1] and Andrew M. McDonald [8]

[1] Queen's Facility for Isotope Research, Department of Geological Sciences and Geological Engineering, Queen's University, Kingston, ON K7L 3N6, Canada; archiba@queensu.ca
[2] Arthur B. McDonald Canadian Astroparticle Physics Research Institute, Department of Physics, Engineering Physics & Astronomy, Queen's University, Kingston, ON K7L 3N6, Canada
[3] School of Earth and Ocean Sciences, University of Victoria, Victoria, BC V8P 5C2, Canada; gsimandl@uvic.ca
[4] Elemental Scientific Lasers, LLC, 685 Old Buffalo Trail, Bozeman, MT 59715, USA
[5] Geological Survey of Canada, Natural Resources Canada, Sidney, BC V8L 4B2, Canada; suzanne.paradis@nrcan-rncan.gc.ca
[6] Next Environmental Ltd., Burnaby, BC V5N 4N4, Canada
[7] Geological Survey of Canada, 601 Booth St, Ottawa, ON K1A 0E8, Canada; alexandre.voinot@nrcan-rncan.gc.ca
[8] Harquail School of Earth Sciences, Laurentian University, Sudbury, ON P3E 2C6, Canada; amcdonald@laurentian.ca
* Correspondence: m.leybourne@queensu.ca

Abstract: Fersmite ([Ca,Ce,Na][Nb,Ta,Ti]$_2$[O,OH,F]$_6$) from the Mount Brussilof magnesite deposit, British Columbia, Canada occurs as accessory brittle, black, submetallic to vitreous lustre, acicular to platy crystals up to 2 cm long, developed in sparry dolomite, which lines cavities in sparry magnesite. Fersmite also occurs as smaller crystals (<3 mm) enclosed by dolomite, where it is commonly fractured or broken, formed during the final stage of dolomite crystallisation. Electron microprobe (WDS) major element data indicate that the grains confirmed to be fersmite by X-ray diffraction contain >50% Nb and are atypically Ta-poor. Fersmite contains significant U and Th (up to 4700 ppm and 6 wt.%, respectively) and therefore is a viable mineral for U-Pb geochronology. A series of laser-ablation inductively coupled plasma mass spectrometry (LA-ICP-MS) spot analyses and maps were collected on fersmite grains. Although the fersmite grains have considerable common Pb and have experienced Pb loss, the U-Pb spot data suggest growth or pervasive resetting at ca. 190 Ma. Some ^{40}Ar/^{39}Ar ages (two of four samples) are consistent with the ~190 Ma U-Pb date. Electron microprobe and LA-ICP-MS mapping indicate that the fersmite is middle to heavy rare earth element-rich. The ~190 Ma fersmite age estimate provides an approximate upper time constraint on the age of sparry magnesite mineralisation, sparry dolomitisation, and, indirectly, on the formation of MVT deposits in the Kicking Horse Rim area and possibly elsewhere in southeastern British Columbia.

Keywords: fersmite; Mount Brussilof; magnesite; MVT deposits; timing of mineralisation; U-Pb dating; Ar-Ar dating

check for updates

Academic Editor: Huan Li

Received: 9 December 2024
Revised: 19 January 2025
Accepted: 22 January 2025
Published: 27 January 2025

Citation: Leybourne, M.I.; Simandl, G.J.; Petrus, J.A.; Paradis, S.; Akam, C.; Voinot, A.; Archibald, D.; McDonald, A.M. U-Pb Geochronology of Fersmite: Potential Time Constraints on Magnesite Formation, Sparry Dolomitisation, and MVT Pb-Zn Mineralisation in SE British Columbia, Canada. *Minerals* **2025**, *15*, 128. https://doi.org/10.3390/min15020128

Copyright: © 2025 by the authors. Licensee MDPI, Basel, Switzerland. This article is an open access article distributed under the terms and conditions of the Creative Commons Attribution (CC BY) license (https://creativecommons.org/licenses/by/4.0/).

1. Introduction

The age of magmatic and magmatic-hydrothermal deposits is relatively easy to determine, as they commonly form readily datable minerals at or near the time of ore formation,

including zircon, apatite, and monazite. However, for sediment-hosted massive sulfide deposits (SHMS; aka sedimentary exhalative or SEDEX), Mississippi Valley-type deposits (MVT), and sediment-hosted Cu deposits, datable minerals are rare to absent because these deposits form at lower temperatures, and many of them are not coeval with igneous activity.

The Mount Brussilof magnesite deposit, currently mined, is located 40 km northeast of Invermere, British Columbia, Canada (Figure 1). There is a spatial, structural, and geological relationship between typical MVT deposits in southeastern British Columbia (e.g., Monarch, Kicking Horse, Shag, and Hawk Creek) and the Mount Brussilof magnesite deposit. They are hosted by the Middle Cambrian Cathedral Formation within the Kicking Horse Rim, along the projection of the Cathedral Escarpment (Figure 1). Field and textural (paragenetic) relationships provide relative timing of the late sparry dolomitisation and magnesite ore, and both are younger than Middle Cambrian, the stratigraphic age of the Cathedral Formation hosting these deposits [1–3].

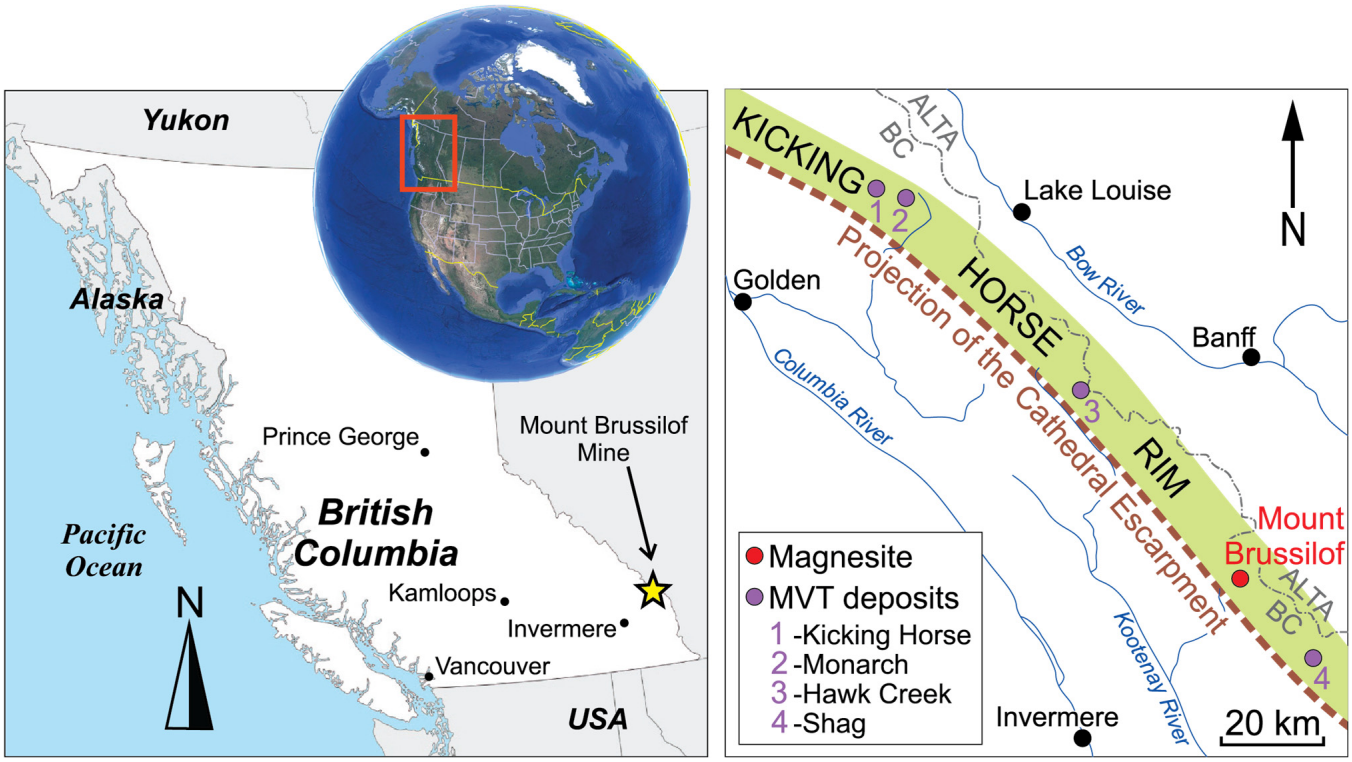


Figure 1. Location of the Mount Brussilof magnesite deposit, British Columbia, Canada. The locations of MVT deposits within the Kicking Horse Rim are also shown.

Two main theories addressing the origin of sparry magnesite along the Kicking Horse Rim are as follows: (i) magnesite replaced permeable dolomitised carbonates because of hydrothermal fluid–rock interaction, essentially an analogue to an extreme case of dolomitisation [4]; and (ii) recrystallisation of a magnesia-rich protolith consisting of fine-grained hydromagnesite, huntite precursors deposited in a marine evaporitic setting and converted to magnesite during a diagenetic or very low-grade metamorphic event [2,5].

At the Mount Brussilof deposit, sparry magnesite is cut by sparry dolomite [3], and fersmite ($[Ca,Ce,Na][Nb,Ta,Ti]_2[O,OH,F]_6$) is hosted by the latter. The fersmite age indirectly constrains the upper age of sparry magnesite ore and sparry dolomite. Should all sparry dolomite in southeastern British Columbia be of the same age, or should fersmite be hosted by the latest generation of sparry dolomite, then the fersmite age would also constrain the age of MVT Zn-Pb, REE-fluorite, and magnesite mineralisation in the region.

Laser-ablation inductively coupled plasma mass spectrometry (LA-ICP-MS) is increasingly used widely as a technique suitable for in situ U-Pb geochronology, e.g., [6,7]. It has been successfully applied to many different minerals [8], including zircon, apatite, titanite, and rutile [9], including minerals rich in common Pb such as calcite, e.g., [10], but to our knowledge, never fersmite. Typically, LA-ICP-MS analyses require calibration via a reference material of known composition that is preferably matrix-matched to the unknown. Thus, the main obstacle to accurate and precise fersmite geochronology by LA-ICP-MS is the lack of such a fersmite reference material. However, McFarlane [11] demonstrated that allanite could be satisfactorily U-Pb dated by using NIST 610 (a synthetic doped glass) [12] for calibration. Here, the approach of McFarlane [11] is applied to fersmite for the first time and is also shown to reproduce known ages of a rutile reference material.

The main objectives of this study are to (1) describe the Mount Brussilof fersmite occurrence, (2) define the relationship between fersmite and sparry magnesite and dolomite, (3) develop the methodology to date fersmite, (4) compare the results with age dates on muscovite from the same locality, and (5) use radiogenic dating in combination with paragenetic relationships to indirectly constrain the timing of sparry magnesite and dolomite.

2. Regional Geological Setting

The Mount Brussilof magnesite deposit is located along the NNW-SSE trending Kicking Horse Rim (Figure 1 [13,14]). The southwestern edge of the Kicking Horse Rim, a paleo-topographic high, coincides with the Cathedral Escarpment [15–17]. The rocks northeast of the escarpment, including the Middle Cambrian Cathedral Formation, which hosts the Mount Brussilof magnesite deposit, were deposited in a shallow marine environment, whereas the rocks of the Chancellor Group that outcrop southwest of the escarpment were deposited in a basinal environment [4,18].

In the Mount Brussilof area, the projection of the Cathedral Escarpment coincides with a 'faulted facies change' as mapped by Leech [19] and reinterpreted by [20]. The Mount Brussilof magnesite mine is located 200 m or less from the projection of the Cathedral Escarpment. Faults coinciding with the Cathedral Escarpment, including the Mitchell River fault, may have channeled hydrothermal fluids responsible for magnesite formation or recrystallisation, sparry dolomitisation, and, ultimately, fersmite crystallisation.

3. Analytical Methods

Samples were collected from a small (<10 m long), irregular porous zone consisting mainly of sugary to sparry dolomite. This zone is enriched in Nb (>1500 ppm), Sr (1500 ppm), Y (90 ppm), Zr (100 ppm), and Th (60 ppm) (unpublished data). The zone is exposed a few metres from a pyrite stockwork in the sparry magnesite. The samples selected for detailed geochemical and geochronological studies consist of black, striated, prismatic fersmite crystals measuring approximately 0.5 to 2.0 mm in length. In other Mount Brussilof samples, goyazite, apatite, xenotime, niobium-bearing rutile, and iron-oxide minerals are commonly spatially associated with fersmite.

From several samples collected from the Mount Brussilof magnesite deposit, four polished thin sections were produced: MB-16-01, MB-16-02A, MB-16-02B, and MB-16-02C. In the polished, thin sections, black, striated grains were selected for analysis. Laser-ablation inductively coupled plasma mass spectrometry (LA-ICP-MS) and electron probe microanalysis (EPMA) wavelength dispersive spectrometry (WDS) data were collected in situ from the polished thin sections. Independently, a concentrate of the black striated grains was produced by crushing and hand-picking under a binocular microscope. Three samples were also disaggregated and sieved to different size fractions (MB-18A, B, and C).

3.1. X-Ray Powder Diffraction

The concentrate of the niobate minerals was analysed at the University of British Columbia, Vancouver, British Columbia, Canada. A corundum mortar and pestle was used to grind the concentrate sample, and the resultant powder was dispersed onto a zero-diffraction quartz plate using ethanol. X-ray powder-diffraction data were collected as a continuous scan over the range 3–80° 2θ using Co Kα radiation on a Bruker (Billerica, MA, USA) D8 Focus Bragg–Brentano diffractometer equipped with a Fe-monochromator foil, 0.6 mm (0.3°) divergence slit, incident- and diffracted-beam Soller slits, and a LynxEye detector. The long fine-focus Co X-ray tube was operated at 35 kV and 40 mA, using a take-off angle of 6°. The X-ray powder diffraction of the concentrate was needed to confirm the identity of the Ca-niobate because fersmite has a similar Nb/Ca value to vigezzite (an aeschynite-group mineral with a generalised formula $[Ca,Ce][Nb,Ta,Ti]_2O_6$).

3.2. Scanning Electron Microscopy

An FEI (now ThermoFisher Scientific; Waltham, MA, USA) mineral liberation analysis (MLA) Quanta 650 FEG (field emission gun)-environmental scanning electron microscope (ESEM) at the Queen's Facility for Isotope Research (QFIR) at Queen's University was used to characterise and create high-resolution backscattered electron (BSE) images of the polished thin sections (Supplementary Materials). SEM analysis by energy dispersive spectrometry (EDS) was used to confirm the identification of fersmite and to identify and document mineralogy and mineral associations. MLA images were generated to identify the minerals present. The QFIR mineral Energy Dispersive Spectrometry (EDS) library was used to create false-colour mineral maps and determine modal mineralogy [21] (Supplementary Table S1, Supplementary Figures S1–S3).

3.3. EPMA Analyses

Selected fersmite grains were analysed by EPMA using a Cameca SX50 (Gennevilliers, France) at the Central Analytical Facility, Laurentian University, Sudbury, Ontario, Canada. Operating conditions were 20 kV and 20 nA using a focused beam and WDS acquisition, and a PAP correction was applied. Standards used were APS25 (F), Albite (Na), Wake Diopside (Ca), $CaTiO_3$ (Ti), YPO_4, (Y), $MnNb_2O_6$ (Nb), $CePO_4$ (Ce), and $LiTaO_3$ (Ta). The count times were 15 s (F, Y, Ce, Ta) and 30 s (Na, Ca, Ti, Nb).

3.4. Laser-Ablation Inductively Coupled Plasma Mass Spectrometry

The U-Pb and trace element contents of fersmite were determined by LA-ICP-MS at Laurentian University. The measurements were made in situ by ablating the grains with a Resonetics (now Applied Spectra Instruments, West Sacramento, CA, USA) RESOlution M-50 laser-ablation system employing a Coherent CompexPRO ArF 193 nm wavelength, 20 ns pulse duration laser, and a Laurin Technic two-volume laser ablation cell [22]. Ablation took place in ultra-pure He, flowing at 650 mL/min. The He and ablation aerosol were combined with N_2 (6 mL/min) and Ar (750 mL/min) immediately outside the ablation cell and transferred to the torch of the ICP-MS by approximately 3 m of tubing with a signal smoothing device. The ablated material was analysed by a Thermo X-Series II ICP-MS operating with a forward power of 1450 W. Prior to each session, the ICP-MS was tuned by ablating NIST612 to maximise sensitivity and to minimise oxide production (<0.5%) and yield Th/U~1. Different isotopes were analysed in each session, as the preceding measurements showed significant trace element variation. Dwell times during analysis were 5–10 ms for major and trace elements and 20–40 ms for U-Th-Pb (^{206}Pb: 30 ms, ^{207}Pb: 40 ms, ^{208}Pb: 20 ms, ^{232}Th: 20 ms, ^{238}U: 30 ms). Spot data were collected using a beam diameter of 48 μm, repetition rate of 6 Hz, and fluence of 5 J/cm^2.

As the chemistry and U-Pb systematics of the initial spot analyses appeared to be complex, several grains were laser-mapped to reveal elemental relationships in more detail. The maps were acquired by ablating a series of parallel and adjacent traverses over the regions of interest [7]. To improve the spatial resolution, a smaller spot size of 14 μm was used with a scan speed of 7 μm/s and repetition rate of 8 Hz.

Calibration was carried out using certified reference materials NIST610, NIST612, and BHVO-2G, as well as U-Pb rutile reference material RZ3 [23], each of which was analysed before, after, and periodically during each analytical session. The data were processed using Iolite version 3.4 [24]. The trace element contents were calculated using the "TraceElements_IS" data reduction scheme of Iolite with NIST610 as the external standard and Nb (53.28 wt.%; mean of WDS data) as the internal standard. The U-Pb data were processed using the 'VizualAge' data reduction scheme of Petrus and Kamber [25]. Note that using RZ3 as the reference material was not judged practical because (1) it is not matrix-matched; (2) it has very low U and Th contents, further complicating its use; and (3) it is not as homogeneous as NIST610 glass.

3.5. Laser Ablation Sr Isotopic Analyses

In situ analyses of Sr isotopes in dolomite were based on the procedures described in ayer, Jugo [26]. Briefly, grain mounts of dolomite were from representative fersmite three-size fractions. In situ Sr isotope analyses were performed by laser-ablation multi-collector inductively coupled plasma mass spectrometry (LA-MC-ICP-MS) at QFIR, Kingston, Ontario, Canada. Analyses employed a 193 nm excimer laser (Elemental Scientific NWR193; Omaha, NE, USA) interfaced with a ThermoFisher Neptune MC-ICP-MS. Operating conditions were a 150 μm diameter laser spot, a repetition rate of 10 Hz, a beam energy density of ~2.3 J/cm^2, and 120 s per analysis preceded by 60 s of blank analysis. The masses analysed were ^{82}Kr, ^{83}Kr, ^{84}Sr, ^{85}Rb, ^{86}Sr, ^{87}Sr, ^{88}Sr, and ^{44}CaPO, as well as double-charged REE (^{163}Dy^{++}, ^{167}Er^{++}, ^{171}Yb^{++}, ^{173}Yb^{++}, and ^{175}Lu^{++}) using dynamic mode (center mass jumping from 86 to 86.5). The idle time was set to 3.0 s to allow for magnet and amplifiers to settle. The integration time was set to 2.0 s for Kr, Rb, Sr, and Ca and 1.0 s for doubly charged REE. Negative values were set to zero (mainly Kr and REE). Five to ten spot analyses were measured along with a reference material, such as BHVO-2G, BIR-1G, or TB-1G, after every two unknown dolomite analyses. After acquisition, data were corrected for Kr interference (^{84}Kr on ^{84}Sr and ^{86}Kr on ^{86}Sr, calculated from ^{82}Kr and ^{83}Kr) using the blank analysis for each individual sample (background counts). Data were subsequently corrected for doubly charged REE interference on Rb and Sr (^{85}Rb was corrected for interference of ^{170}Er^{++} and ^{170}Yb^{++}, ^{86}Sr was corrected for interference of ^{172}Yb^{++}, ^{87}Sr was corrected for interference of ^{174}Yb^{++}, and ^{88}Sr was corrected for interference of ^{176}Yb^{++} and ^{176}Lu^{++}). Mass bias on ^{87}Rb/^{85}Rb was calculated using the mass bias of ^{86}Sr/^{88}Sr, measured relative to the ^{86}Sr/^{88}Sr natural value = 0.1196. The ^{87}Sr/^{86}Sr values were then corrected for interference of ^{87}Rb on ^{87}Sr. A time-dependent function was used to correct for the certified values of ^{87}Sr/^{86}Sr values of the standards. This correction was completed using the ^{85}Rb/^{88}Sr measured (y) and ^{87}Sr/^{86}Sr measured subtracted by the certified value of ^{87}Sr/^{86}Sr for the reference materials (TB-1G and BHVO-2G) analysed at the start and end of each analytical session (typically including four samples). BIR-1G was not used for the correction because of lower Sr-Rb concentrations (larger analytical uncertainties) but was used to check the accuracy of the correction calculation. Using linear regressions, the slope (m) and intercept (b) were calculated for each individual analysis, then used to correct for drift over time and differences in the standard ^{87}Sr/^{86}Sr measured values to the true ^{87}Sr/^{86}Sr values. The certified value of ^{87}Rb/^{86}Sr in TB-1G was used to correct for ^{87}Rb/^{86}Sr. This was calculated using natural ratios and average published concentrations

of Sr (1322 ± 52 ppm) and Rb (140 ± 10 ppm) for TB-1G [27]. Based on the difference between the value measured and the true $^{87}Rb/^{86}Sr$ in TB-1G, empirical correction factors were calculated for each analysis (~2.3 to 2.0) and applied to the $^{87}Rb/^{86}Sr$ measured. BHVO-2G analyses yielded an average $^{87}Sr/^{86}Sr$ of 0.703300 ± 0.00037 (1σ) and TB-1G gave an average $^{87}Sr/^{86}Sr$ of 0.705515 ± 0.00018 (1σ).

3.6. $^{40}Ar/^{39}Ar$ Methods

Samples of relatively pure mica were crushed, sized, and washed. The selected mica samples and flux monitors (standards) were wrapped in Al foil and loaded into an 11.5 cm long and 2.0 cm diameter irradiation container, and then irradiated with fast neutrons in position 5C of the McMaster Nuclear Reactor (Hamilton, ON, Canada) for 29 h. Monitors were distributed throughout the irradiation container, and J-values for individual samples were determined by polynomial interpolation of replicate analyses of the standards.

The mineral separates and the monitors were heated in a pure-silica tube (GE214) using a Lindberg furnace. Reactive gases were removed using a heated Ti sponge and a SAES C50 getter. The bakeable, ultra-high vacuum, stainless-steel, argon-extraction system was operated on-line to a substantially modified A.E.I. MS-10 mass-spectrometer running in static mode.

Measured mass-spectrometric ratios were extrapolated to zero-time, corrected for system Ar blanks, normalised to a $^{40}Ar/^{36}Ar$ atmospheric value of 295.5, and corrected for neutron-induced ^{40}Ar from potassium and ^{39}Ar and ^{36}Ar from calcium. Ratios were corrected for the decay of ^{37}Ar and ^{39}Ar during and after irradiation. Dates and errors were calculated using formulae given by Dalrymple,Alexander [28] and the constants recommended by Steiger and Jäger [29]. Errors shown on age spectra represent the analytical precision at 2σ and do not include the error in the age of the flux monitor. The dates are referenced to the LP-6 biotite standard using an age of 128.5 Ma [30]. Using the ^{40}K decay constant of Min,Mundil [31] would increase the dates by ~0.68%.

4. Results

4.1. XRD and SEM

The XRD data for the fersmite samples reported here have been published previously [32]. These data confirmed that the samples are fersmite. Three polished thin sections were also analysed by MLA-SEM to determine modal mineralogy (Supplementary Table S1). The samples are dominated by fersmite (27.35 to 80.21 wt.%) and dolomite (17.82 to 67.59 wt.%), with minor quartz (1.38 to 2.86 wt.%) and several other minerals in trace quantities, including calcite, barite, and apatite (Supplementary Table S1). This table also provides mineral proportions in terms of area percentage, number of grains, and number of particles. In addition to the MLA analyses of the grain separates, backscatter images of fersmite grains indicate that there is significant compositional zonation (Figure 2).

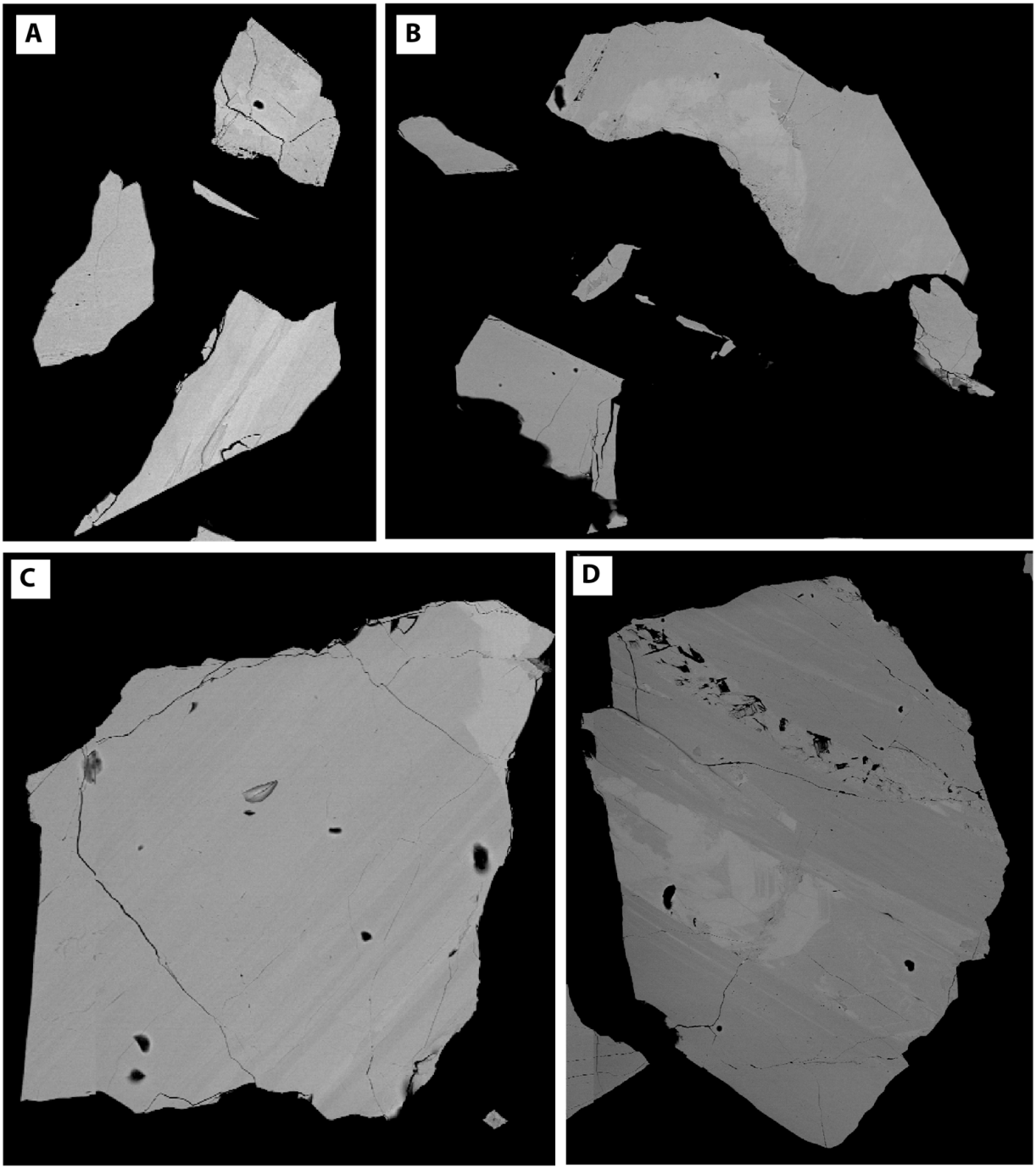


Figure 2. SEM images of individual fersmite grains from MB-18A (**A**), MB-18B (**B**), and MB-18C (**C**,**D**). Note that fersmite grains are clearly zoned in the SEM images.

4.2. EPMA and LA-ICP-MS Analyses of Fersmite

4.2.1. Major Elements

Based on EPMA analyses, Mount Brussilof fersmite is dominated by Nb and lesser Ca. Other key constituents include Ti, Y, and Na (Supplementary Table S2; Figure 3), consistent with the formula for fersmite ($[Ca,Ce,Na][Nb,Ta,Ti]_2[O,OH,F]_6$). Variable totals (Supplementary Table S2) are consistent with variable volatile contents, e.g., F by EPMA ranges up to 0.12 wt.%. Fersmite compositions show an inverse correlation between Nb_2O_5 and TiO_2 and a positive correlation between CaO and Nb_2O_5, consistent with the chemical formula (Figure 3). Yttrium values range from less than detection to 2.04 wt.% Y_2O_3 by

EPMA (average 0.55 wt.%), and from 1.15 to 3.35 wt.% Y_2O_3 by LA-ICP-MS (average 1.92 wt.%; range is 9070 to 26,390 ppm Y).

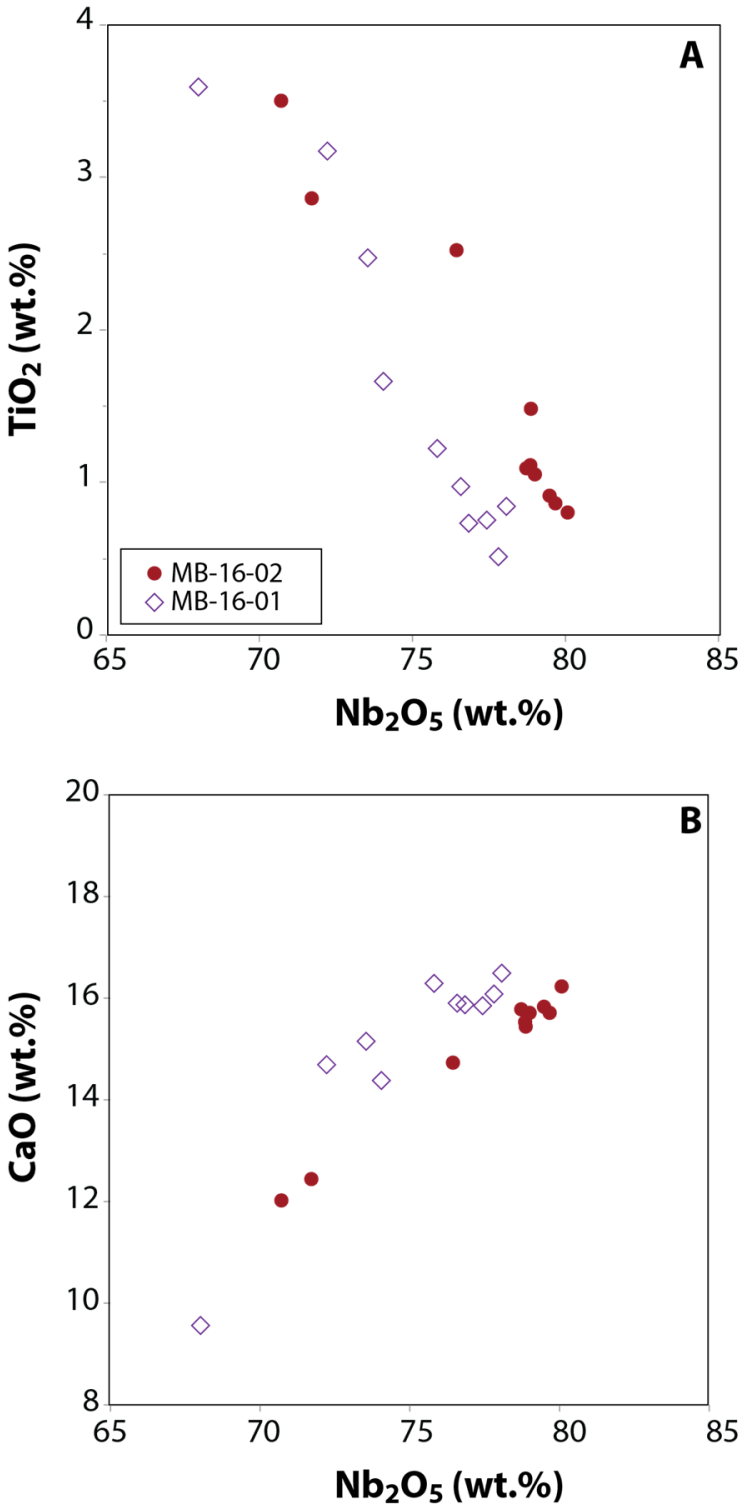


Figure 3. Plots of (**A**) TiO_2 and (**B**) CaO versus Nb_2O_5 for fersmite crystals from samples MB16-01 and MB16-02.

4.2.2. Trace Elements

A number of trace elements were analysed by LA-ICP-MS on the fersmite grains in samples MB16-01 and MB16-02A, B, and C (Figure 4). Tantalum concentrations are remarkably and atypically low in the Mount Brussilof fersmite, essentially below the

detection limit by EPMA. LA-ICP-MS analyses show Ta concentrations that range from 2 to 45 ppm.

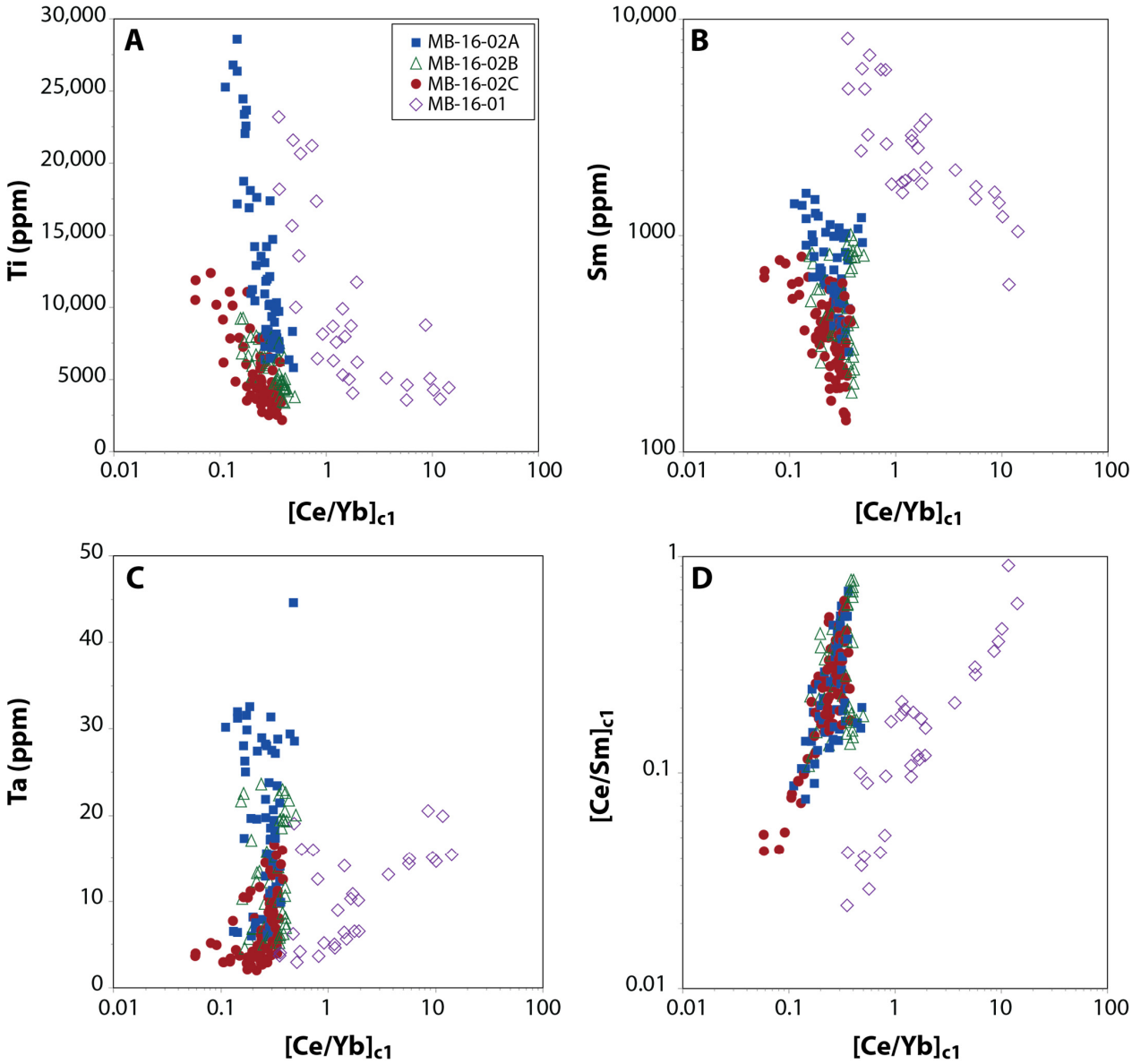


Figure 4. Plots of (**A**) Ti, (**B**) Sm, (**C**) Ta, and (**D**) $[Ce/Sm]_{c1}$ versus $[Ce/Yb]_{c1}$, where c1 refers to C1 chondrite normalised values. Chondrite normalising values from [33].

Uranium and Th values vary up to several thousand ppm, and U shows a strong correlation with ^{206}Pb (r^2 = 0.913; $p < 0.0001$) and Th with ^{208}Pb (r^2 = 0.688; $p < 0.0001$). Concentrations of Pb vary up to ~800 ppm (Supplementary Tables S3 and S4). There is no correlation between U and Th, and all samples overlap on a plot of U versus Th. Although Th and ^{208}Pb show a strong correlation, sample MB-16-02A has lower Th/Pb (65) than sample MB-16-01C (163). Zirconium concentrations are low, ranging from 0.9 to 26 ppm (Supplementary Table S3). Iron concentrations in fersmite are low, ranging from a few thousand ppm to below the detection limit.

4.2.3. REE Patterns

Fersmite has elevated REE concentrations with SREE ranging from 3190 to 20,830 ppm for three samples with all REE analysed and not including Y. The REE patterns for the spot data on three samples are plotted in Figure 5, all of which show double-humped

MREE enrichment. The MREE hump does appear to be shifted to heavier REE compared to fersmite in other deposits in BC [34]. Sample MB-16-01 differs from the other three samples in that the MREE enrichment occurs at lighter REE, such that Sm concentrations in sample MB-16-01 are higher than samples MB-16-02A, B, or C (Figure 4). Sample MB-16-01 is also more HREE depleted with [Ce/Yb]c1 normalised values much higher than the other samples (Figure 4). All samples have low La compared to Ce (i.e., negative La anomalies; Figure 5).

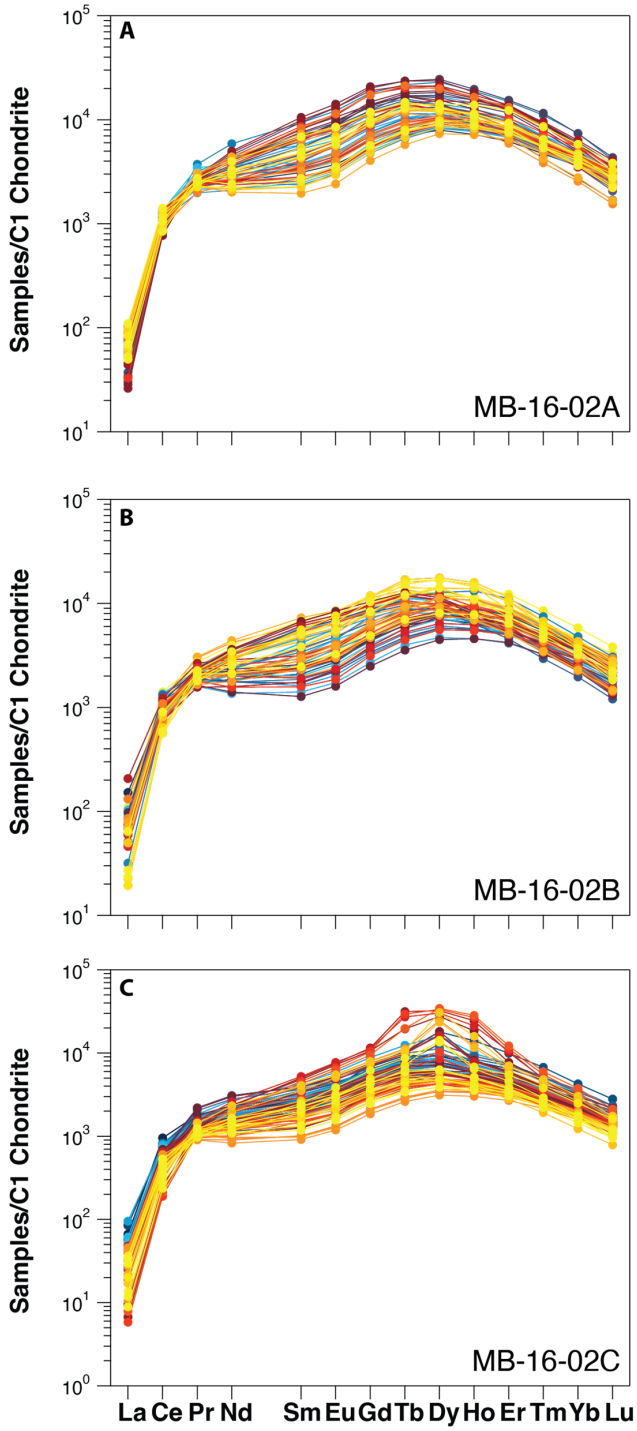


Figure 5. Chondrite-normalised REE plots for MB-16-02A (**A**), B (**B**), and C (**C**), showing MREE enrichment and large depletion in La. MB-16-01 is not plotted, as not all REEs were analysed for that session. Chondrite normalising values from [33].

4.2.4. LA-ICP-MS Mapping of Fersmite

The spot trace element (and U-Pb) data were highly variable, hinting that there may be some interesting spatial distributions that could help constrain mineral growth. A series of maps were acquired to determine this spatial distribution (e.g., Figures 6–8). These maps also have the added benefit that they do not penetrate deep into the mineral and therefore do not suffer from significant downhole fractionation.

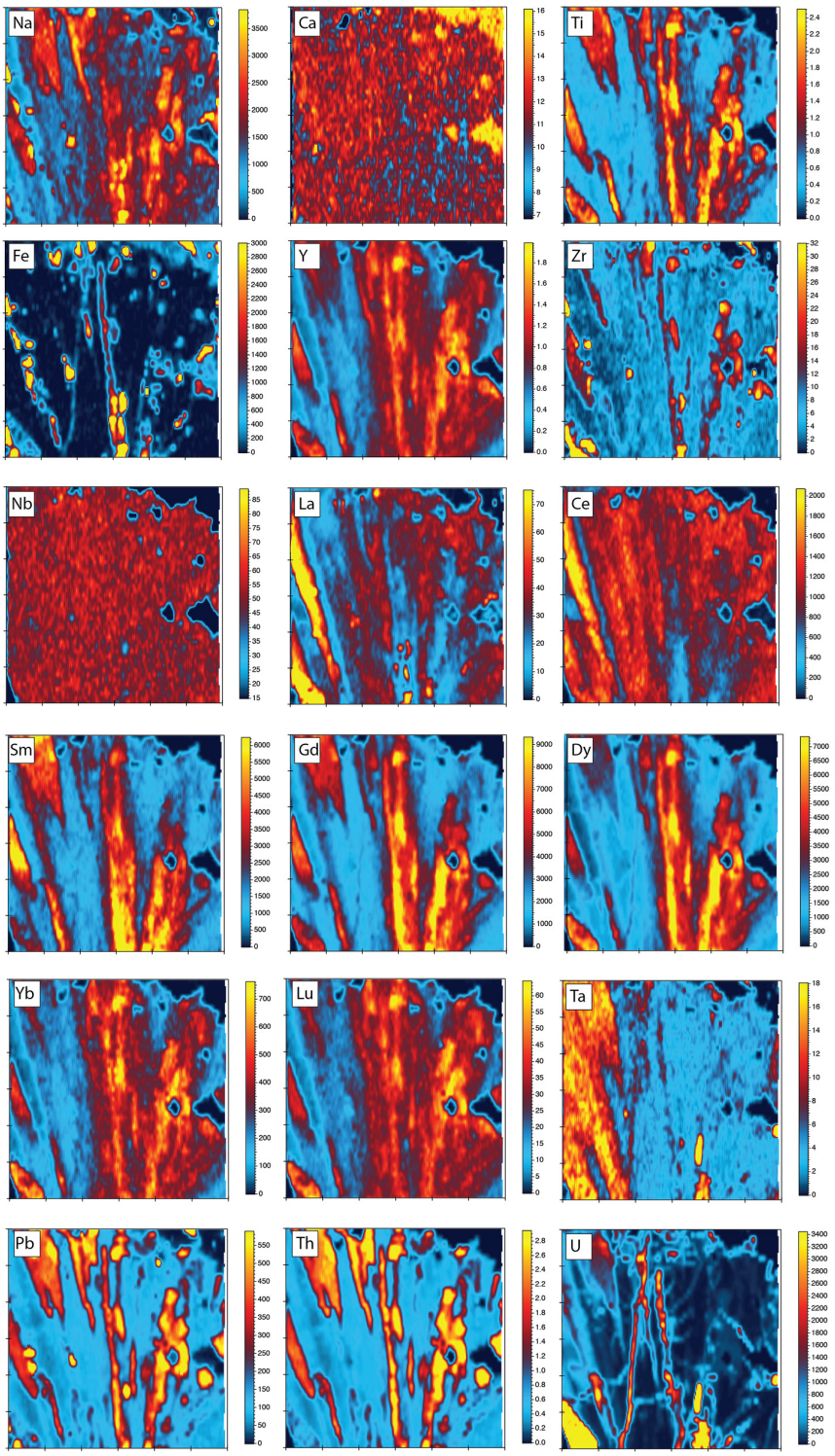


Figure 6. Laser ablation maps of fersmite grain from sample MB-16-01. All analytes are in ppm except Ca, Mg, Ti, Y, and Th, which are in wt.%. The area of each image is 600 µm × 600 µm.

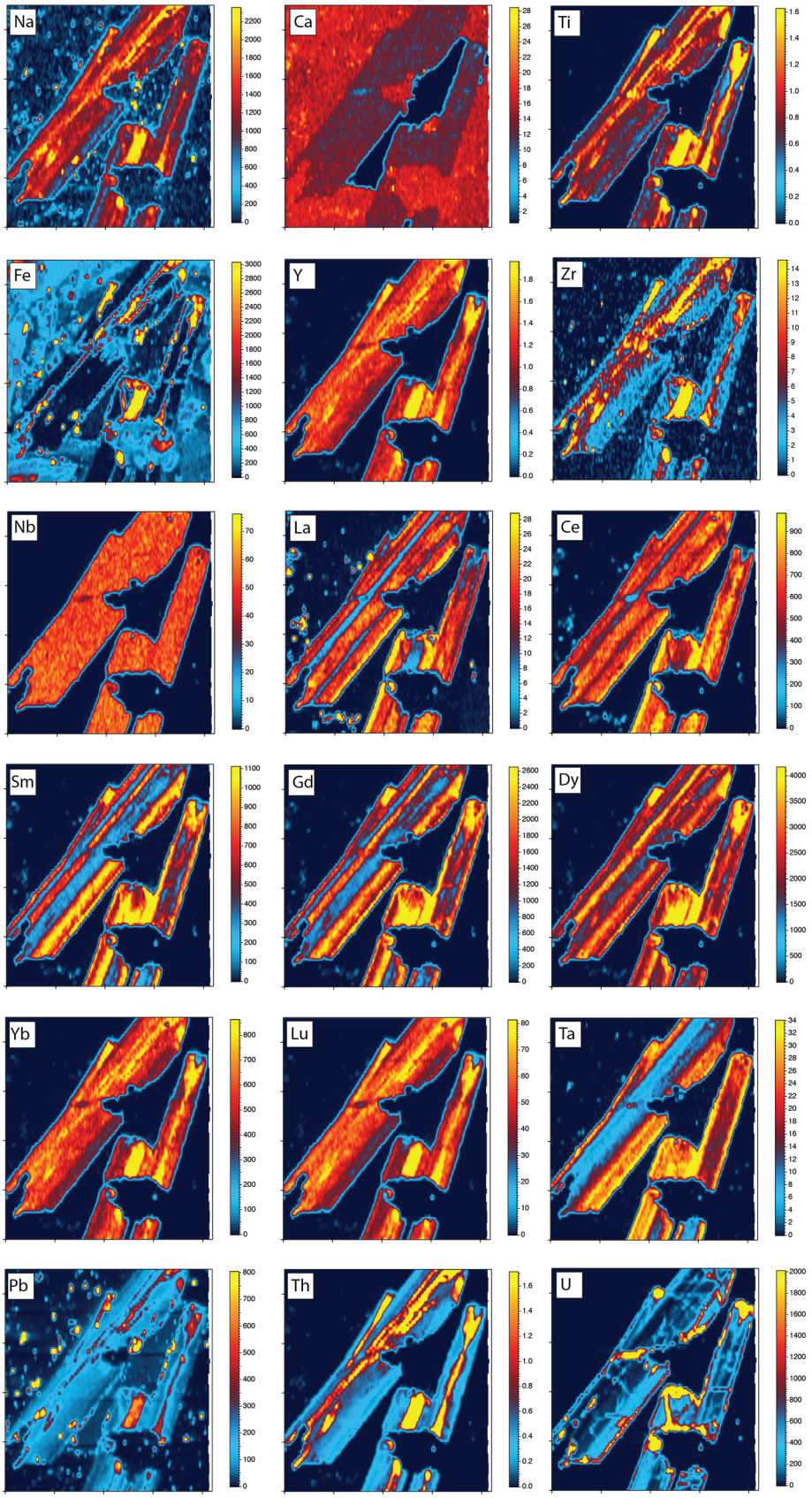


Figure 7. Laser ablation maps of fersmite grain from sample MB-16-02A. All analytes are in ppm except Ca, Mg, Ti, Y, and Th, which are in wt.%. The area of each image is 840 µm × 810 µm.

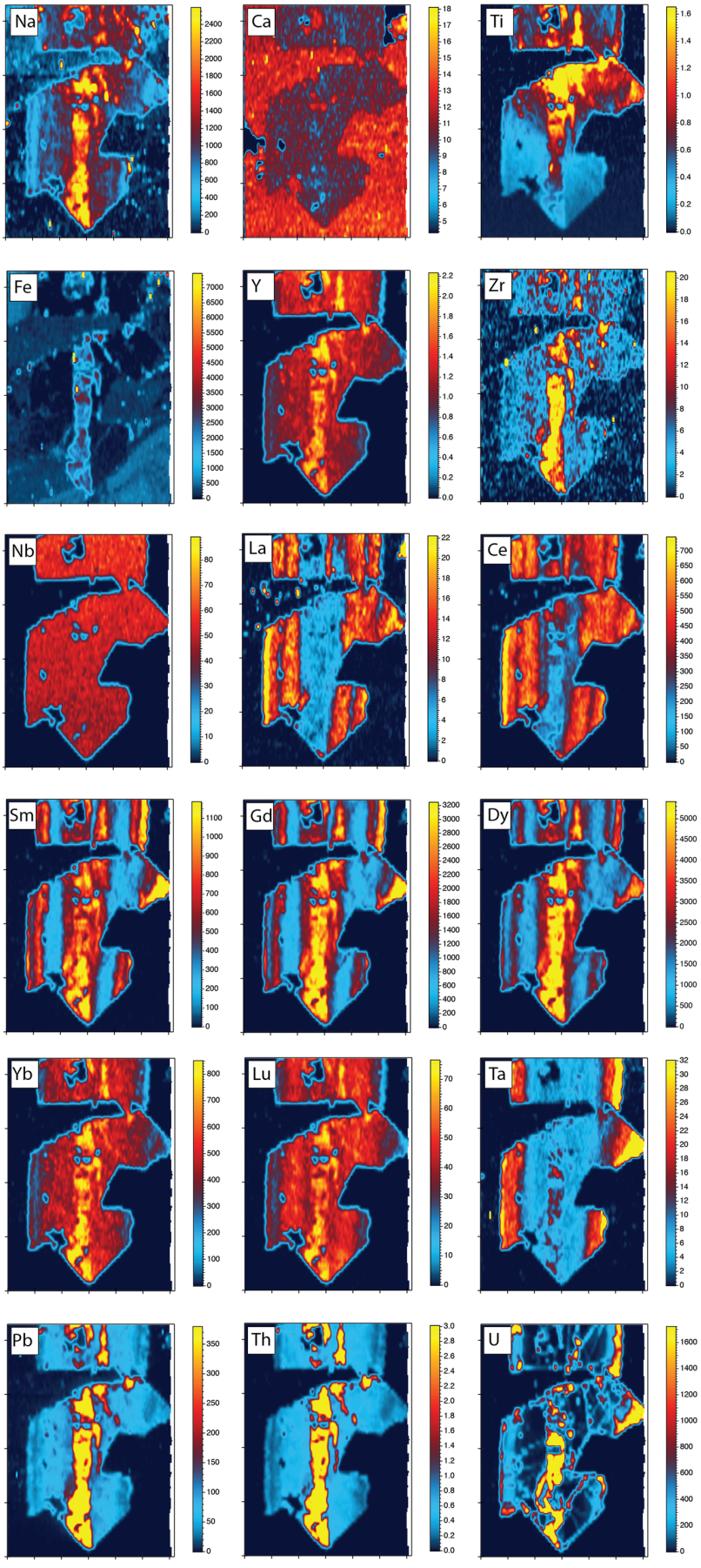


Figure 8. Laser ablation maps of fersmite grain from sample MB-16-02C. All analytes are in ppm except Ca, Mg, Ti, Y, and Th, which are in wt.%. The area of each image is 820 µm × 600 µm.

Compositional maps of fersmite crystals (Figures 6–8) show well-developed zonation in terms of Na, Ti, Fe, Y, the REE, Ta, Pb isotopes (e.g., ^{208}Pb), Th, and U. This systematic zonation explains the relatively high degree of variability in the spot data (Supplementary Table S3) and indirectly confirms the internal consistency of the trace element data (Supplementary Tables S2 and S3).

As outlined in etrus, Chew [7], regions of interest can be generated from laser ablation maps based on a number of different criteria. Here, we generated regions of interest from the three laser ablation maps shown (Figures 6–8; the locations of the regions of interest are shown in Supplementary Figure S4) to extract elemental data representing an average of the region of interest. The REE profiles for the three maps show the difference in sample MB-16-01 in that the MREE enrichment is shifted to lighter REE compared to samples MB-16-02A and C, and that the HREE is somewhat more depleted (Figure 9).

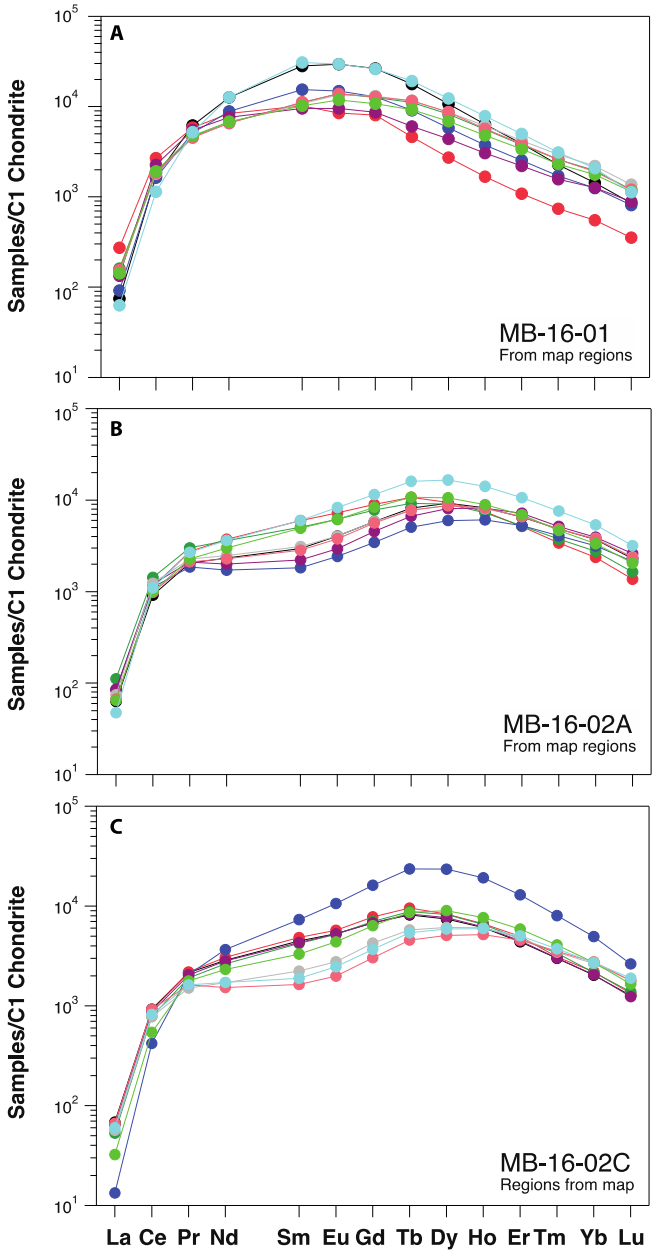


Figure 9. Chondrite normalised REE plots for regions of interest extracted from the LA-ICP-MS maps in Figures 6–8. (**A**) Sample MB-16-01; (**B**) MB-16-02A; (**C**) MB-16-02C. Locations of the regions of interest are shown in the Supplementary Materials. Chondrite normalising values from [33].

4.3. LA-ICP-MS U-Pb Analyses

4.3.1. Reproduction of Rutile Standard RZ3

Typically, LA-ICP-MS U-Pb geochronology employs matrix-matched reference materials to obtain accurate results. There are no such materials for fersmite, so we instead employed the approach that McFarlane [11] applied to allanite dating, more specifically, using NIST610 (a synthetic and well-characterised glass) for calibration with a specialised data-reduction scheme. To demonstrate that this approach is capable of reproducing the known age of an oxide, we analysed RZ3 rutile [23]. For the conditions used in this study, the ablation of rutile and NIST610 were sufficiently different such that the downhole fractionation model determined for U-Pb from NIST610 did not adequately compensate for this effect in rutile. However, if we limit the data to the first half of each spot (i.e., when the hole is shallow), the age of RZ3 is reproduced within uncertainty (Figure 10) i.e., we derived an age of 1810 ± 40 Ma compared to the accepted value of 1780 ± 10 Ma [23].

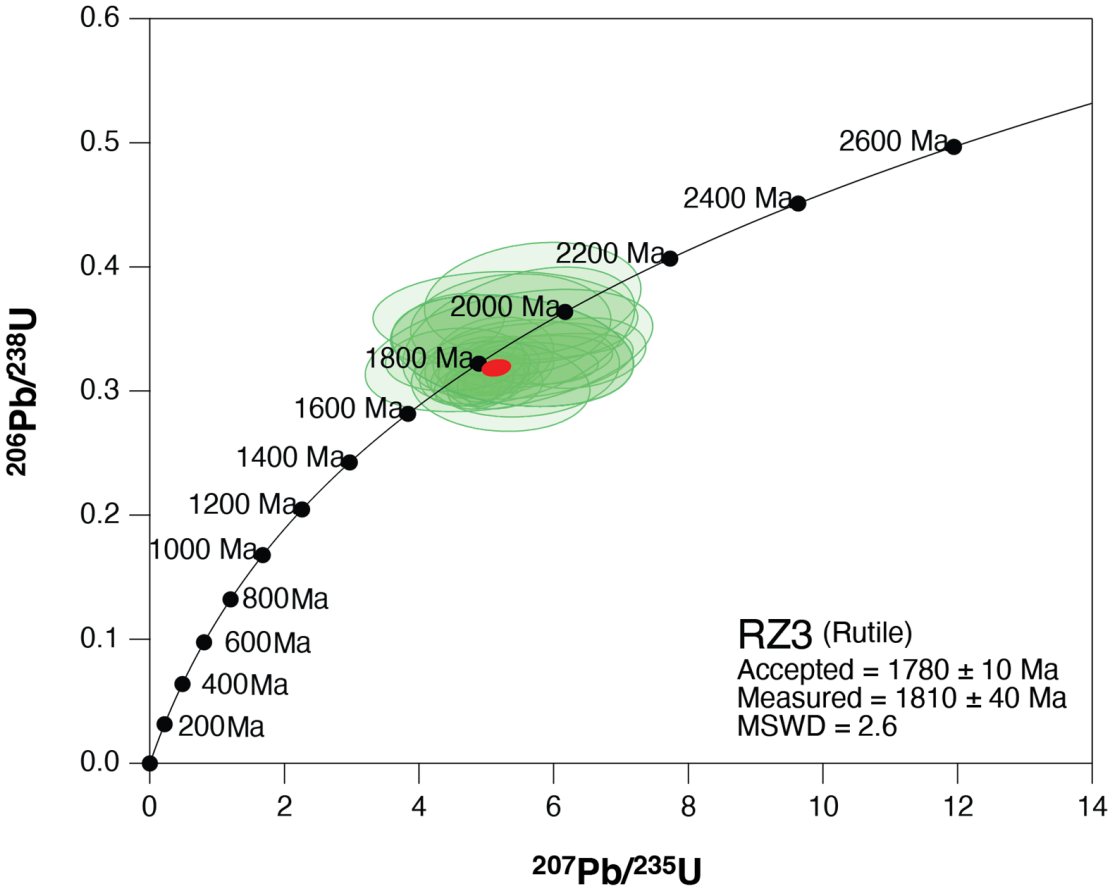


Figure 10. Concordia diagram showing the calculated 'concordia age' for RZ3 [23] when using NIST610 as a reference material as in [11].

4.3.2. Remaining Downhole Fractionation

Because the downhole fractionation model from NIST610 was not successful in correcting for downhole fractionation in rutile, this was also a concern for fersmite. To check whether this issue prevails and to what extent, the average $^{206}Pb/^{238}U$ age and $^{207}Pb/^{206}Pb$ age as a function of time (depth) were plotted for each of the grains from sample MB-16-02B. Because the $^{206}Pb/^{238}U$ age varies with depth and the $^{207}Pb/^{206}Pb$ age does not, downhole fractionation remains an issue for the fersmite, and we therefore restricted the data integrated to the first half of each analysis, as this was successful for the RZ3 rutile.

4.3.3. Concordia Diagrams

Tera–Wasserburg concordia diagrams for each of the samples are shown in Figure 11 and are combined in Figure 12. Recalling that concordant data at ca. 190 Ma would be pulled up towards a y-intercept of 0.834 (common Pb composition from terrestrial Pb evolution model at 190 Ma), and Pb loss tends to pull data to higher $^{238}U/^{206}Pb$ (to the right), it appears that all the data fit well with a ca. 190 Ma event. However, due to the high degree of scatter and the unknown amount of uncompensated downhole fractionation, a more robust/reliable age cannot be determined from these data alone. Additionally, because excess downhole fractionation is more likely to pull data towards lower $^{238}U/^{206}Pb$ values, the estimate of 190 Ma may be slightly high.

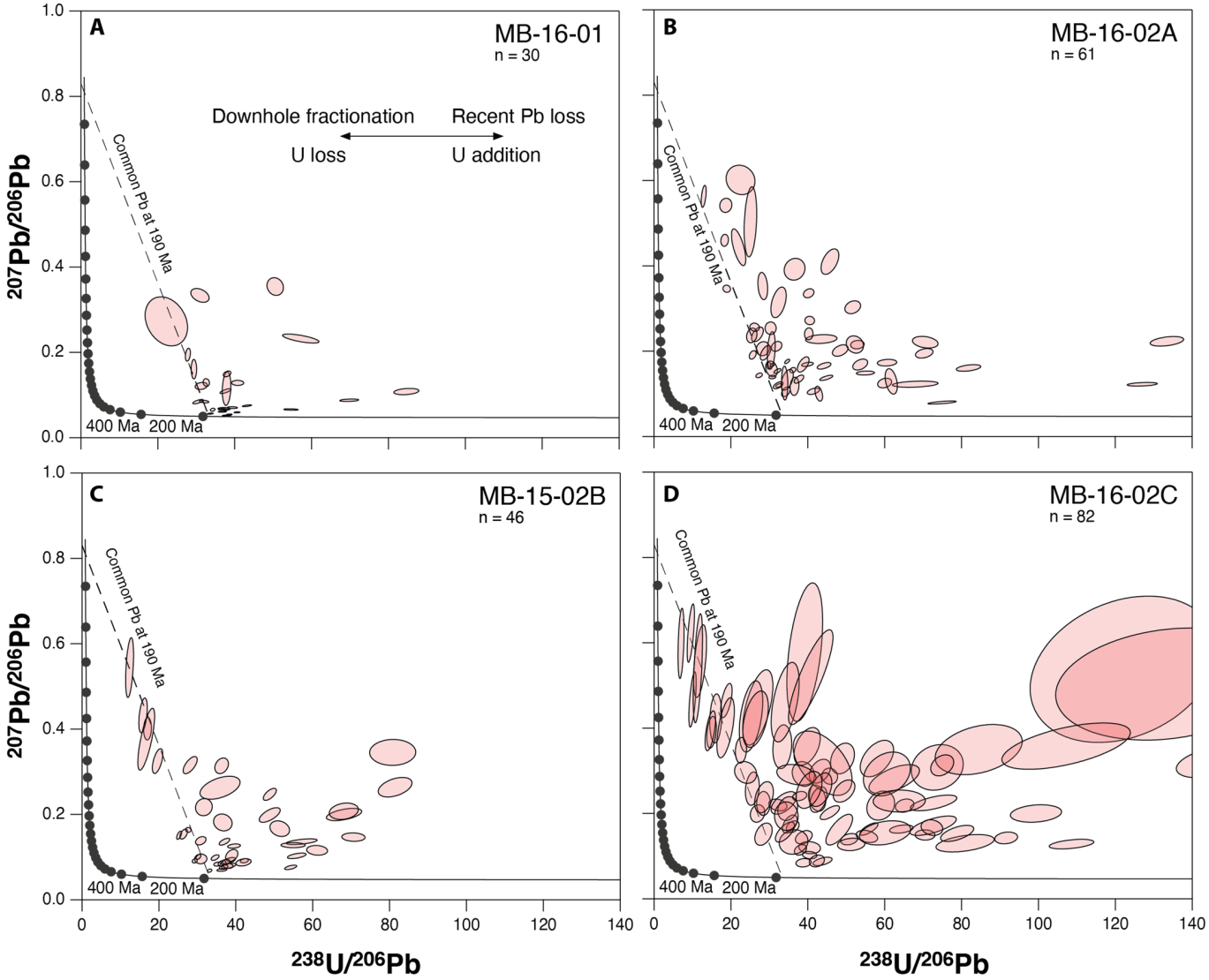


Figure 11. Tera–Wasserburg concordia diagrams for each of the samples analysed. A reference line joining 190 Ma to the common Pb composition at 190 Ma is shown (dashed line). Note that Pb loss would pull data to the right (higher $^{238}U/^{206}Pb$), and downhole fractionation tends to pull data to the left (lower $^{238}U/^{206}Pb$). (**A**) Sample MB-16-01; (**B**) MB-16-02A; (**C**) MB-16-02B; (**D**) MB-16-02C. All of the data seem to support a major event at ca. 190 Ma; however, no robust age can be determined from these data.

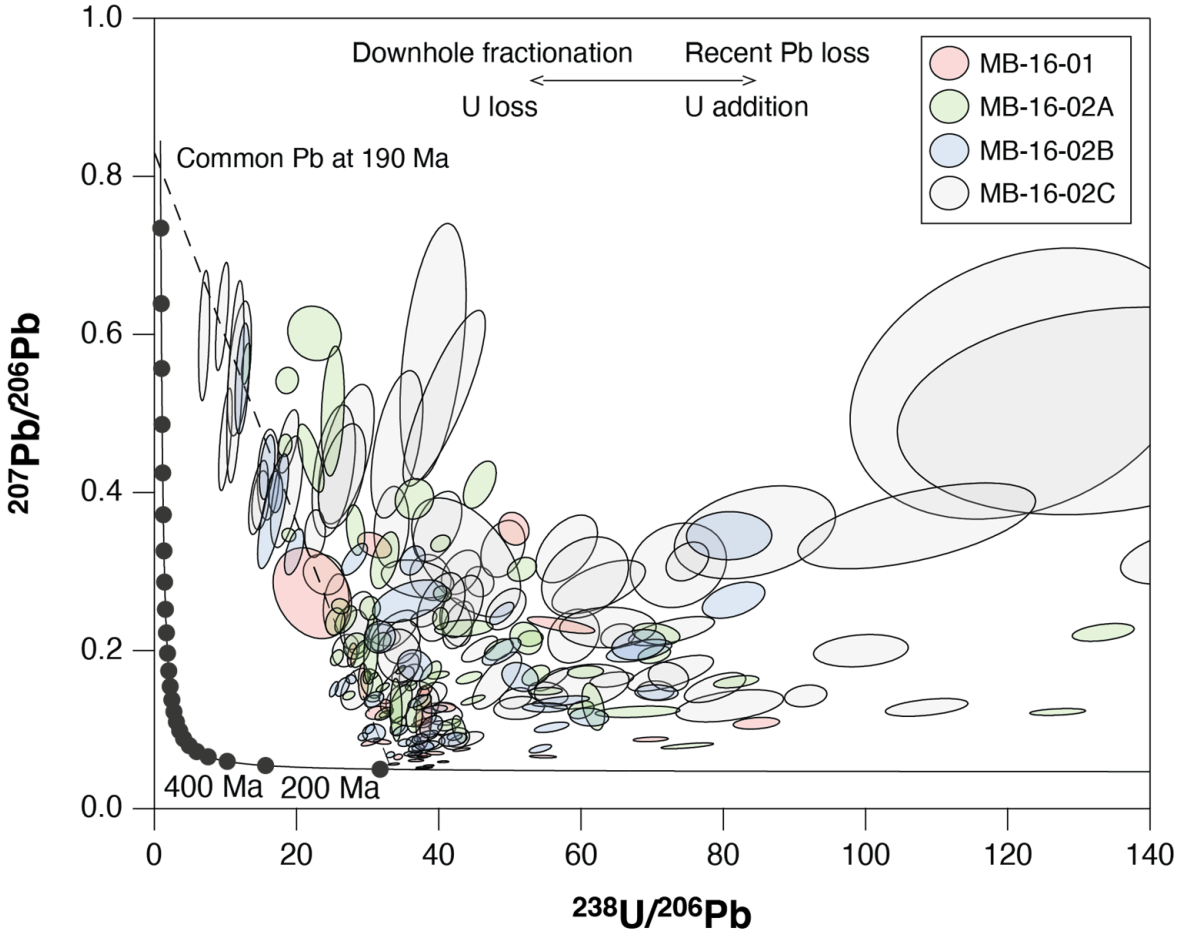


Figure 12. Tera–Wasserburg concordia diagram for each of the samples analysed, plotted together with different colours per sample.

4.4. $^{40}Ar/^{39}Ar$ Dating

Two green micas and two rose micas were analysed in this study (Supplementary Table S5) in 1992; however, the data were not published until now. Sample 90-VUG-1 is coarse-grained, pale green mica in flakes up to 3 mm in diameter. This coarse mica was collected less than 3 metres from the fersmite occurrence and post-dates sparry dolomite, which is lining the vugs and has an age of 190 ± 0.5 Ma. The pink fine-grained mica from the same sample intergrown with sparry dolomite (90-P-Rose Mica) has a similar age of 208 ± 0.91 Ma. Other samples are aggregates of very fine-grained mica. The data from these samples do not show a consistent age, with indicated plateau ages from 322 ± 2.3 to 248 ± 1.9 Ma (Figure 13).

4.5. LA-MC-ICP-MS Sr Isotopes

Twenty grains of fersmite were laser ablated for their Sr isotopic composition. Three certified reference materials were also analysed: BHVO2G, BIR1G, and TB1G (Supplementary Table S6). The average data for the three certified reference materials are systematically slightly low (0.025% lower) compared to the accepted values (Supplementary Table S6). These differences are not considered significant in the context of the overall variation in the $^{87}Sr/^{86}Sr$ values of the samples, so the data are presented as analysed. Strontium isotope values range from 0.707988 to 0.728857, with initial ratios (calculated at 190 Ma) ranging from 0.706115 to 0.728520 (Figure 14).

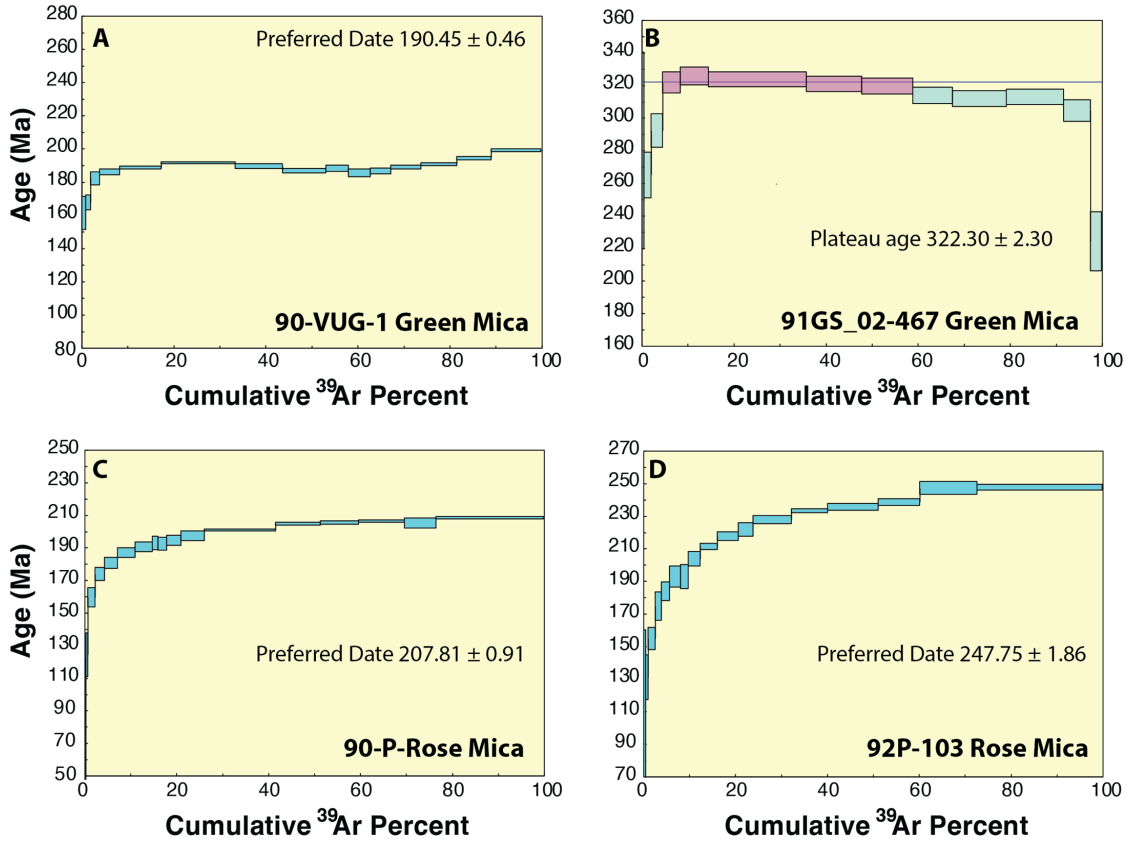


Figure 13. $^{40}Ar/^{39}Ar$ age spectra for mica samples from Mount Brussilof. Mica in (**A**) is coarse grained. Micas in (**B**–**D**) are fine-grained, but (**C**) was analysed as mm-size chips, whereas (**D**) consisted of ~200 µm flakes. The preferred date in (**A**) is the weighted mean of steps 6 and 7. The two highest temperature steps were used for (**C**,**D**). (**A**,**C**) were separated from the same rock.

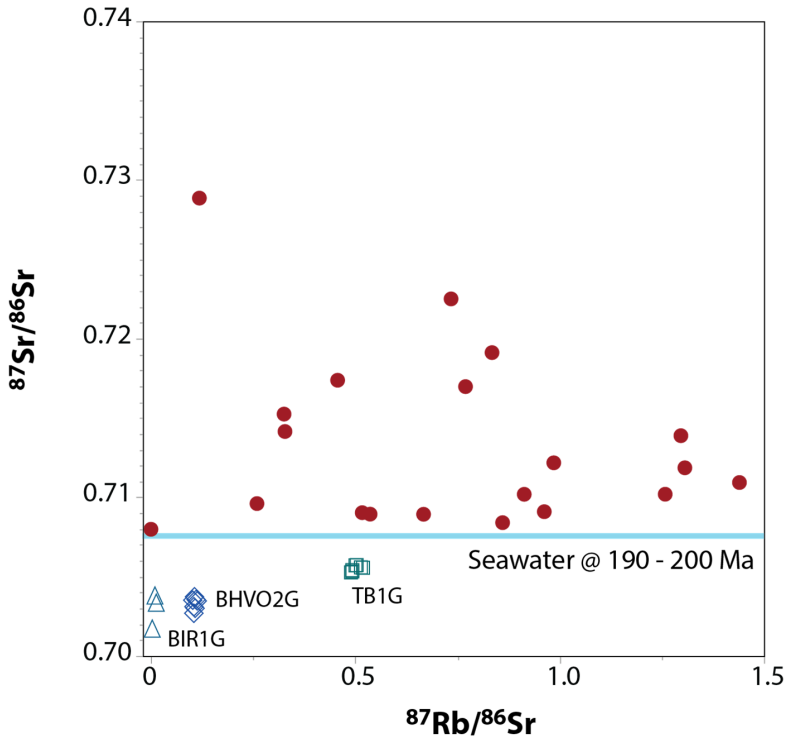


Figure 14. $^{87}Sr/^{86}Sr$ versus $^{87}Rb/_{86}Rb$ for dolomite intergrown with fersmite from Mount Brussilof. Also shown are seawater $^{87}Sr/^{86}Sr$ values at ~190 Ma.

5. Discussion

The geochemistry and relationship among fersmite, magnesite, and sparry dolomite have been discussed previously [32]. These studies characterised Mount Brussilof fersmite as primary, based on its prismatic crystal form and textural habit. Other occurrences of fersmite in BC are primarily an alteration product of other Nb-rich minerals. Given the morphology of the Mount Brussilof fersmite and its relationship to sparry dolomite and cross-cutting magnesite, we suggest that it is a late feature. At the Mount Brussilof magnesite deposit, fersmite is erratically distributed in a restricted area exposed over less than 30 square meters. The Mount Brussilof fersmite can occur as brittle, black, submetallic to vitreous lustre, acicular to platy crystals up to 2 cm long growing on sparry dolomite lining cavities. More commonly, it occurs as smaller crystals enclosed by a dolomite matrix, commonly fractured or broken during the final stage of crystallisation of the matrix. The patchy to oscillatory zoning of the fersmite (Figures 2 and 6–8) is also consistent with a primary origin.

5.1. Chemical Composition of Fersmite

Before discussing the composition of the Mount Brussilof fersmite, we make a couple of comments regarding the trace element analytical techniques, specifically the LA-ICP-MS analyses. In this study, in the absence of a matrix-matched standard, we used the trace-element data reduction scheme in Iolite with NIST610 as the external standard and Nb as an internal standard (see Methods Section 3). Clearly, fersmite and the NIST glass are not matrix-matched. Balachandar,Zhang [35] discussed the difficulty of using glass standards by LA-ICP-MS to calibrate Nb-rich minerals (in their case, columbite). However, for our study, although the locations of the EPMA spots were different from the LA-ICP-MS spots, we found that elements that were common across both analytical techniques showed the same ranges in composition, e.g., TiO_2 by EPMA ranges from 0.51 to 3.59 wt.% (average = 1.60 wt.%) compared to 0.38 to 4.94 wt.% (average = 1.38 wt.%) by LA-ICP-MS (Supplementary Tables S2 and S3). Similarly, the EPMA and LA-ICP-MS data show similar ranges and averages for CaO (averages of 14.97 and 14.26 wt.%, respectively). Therefore, we conclude that the trace elements concentrations derived by LA-ICP-MS are largely quantitative.

5.2. REE Composition of Fersmite

Fersmite is a euxenite group mineral; consequently, it preferentially incorporates Y and HREE in its crystal structure relative to LREE [36–38]. The Mount Brussilof fersmite chondrite-normalised patterns are smooth, convex-upward (i.e., middle-REE enriched), and enriched in the HREE. REE patterns from three of the samples show generally similar patterns with smaller variations in the LREE than the MREE and HREE (Figure 5). The normalised REE patterns are similar in shape to fersmite hosted by the Aley Carbonatite in British Columbia, albeit with lower LREE and some MREE. The maximum of the Mount Brussilof fersmite chondrite-normalised REE distribution is shifted towards heavier REE relative to the REE distribution corresponding to secondary fersmite from the Aley Carbonatite. There are several possible explanations that may be responsible for this shift, the simplest and most likely being that the fluids at Mount Brussilof had higher HREE/LREE values than the Aley carbonatite mineralising system (carbonatites typically have higher LREE/HREE than other rocks).

5.3. Compositional Maps of Individual Fersmite Crystals

The main constituent of Mount Brussilof fersmite is Nb. Other key constituents include Ca, Ta, and Ti. Compositional maps of fersmite crystals (Figures 6–8) show well-

developed zonation in terms of Na, Ti, Fe, Y, all REE, Ta, Pb (e.g., ^{208}Pb), Th, and U. This systematic zonation explains the relatively high degree of variability in the spot data (Supplementary Table S3). The compositional maps suggest an evolving mineralising system over the time of fersmite crystallisation. Zonation trends may be highly relevant when systematically comparing textural and chemical compositions of fersmite from Mount Brussilof to fersmite derived from pegmatites, peralkaline intrusions, carbonatites, and other geological environments.

5.4. Concordia Diagrams and Timing of Fersmite Formation

A summary Tera–Wasserburg concordia diagram derived from data in Supplementary Table S4 is shown in Figures 11 and 12. Recalling that concordant data at ca. 190 Ma would be pulled up towards a y-intercept of 0.834 (common Pb composition from terrestrial Pb evolution model at 190 Ma), and Pb loss or U addition tends to pull data to higher ^{238}U/^{206}Pb (to the right), all the data fit well with a ca. 190 Ma event. Given the greater mobility of U in crustal fluids, U addition is more likely than Pb loss [39]. The U-Pb age of 190 Ma determined from these data provides an approximate and likely upper time limit on the fersmite-forming event. Alternatively, a large amount of Pb loss or U gain might imply that there was a major alteration event at 190 Ma that variably reset the fersmite and perhaps also partially reset the dolomite, resulting in variable Sr isotope compositions. However, the morphology of the fersmite suggests that they are primary and not a result of secondary recrystallisation of a previously formed niobate mineral, as is the case for fersmite in other locations in the region [32].

The geometry of the samples with respect to the concordia in Figures 11 and 12 is like other minerals with elevated U in the structure, albeit with much more scatter than is typical. For example, there have been an increasing number of studies that have investigated LA-ICP-MS analyses of carbonate minerals as recorders of age of crystallisation reviewed recently in [38].

5.5. ^{40}Ar/^{39}Ar Dating

The four samples analysed for ^{40}Ar/^{39}Ar did not yield particularly robust ^{39}Ar release plateaus, except for sample 91GS02-467, which has a plateau age of 322 ± 2.30 Ma (54.4% ^{39}Ar released). However, the four samples yielded three potential ages of mica formation: ~322 Ma, 248 Ma, and ~200 to 190 Ma. The latter age is consistent with the age determined by U-Pb dating of the fersmite.

All micas appear to have been overprinted, perhaps in the Late Cretaceous. A basic interpretation is that the micas crystallised at or before the time indicated by the highest temperature steps (for sample 90-VUG-1, this would be ca. 199 Ma) and were later re-heated (to sub-greenschist facies). Without further characterisation of the fine-grained micas with respect to grain size distribution, it is difficult to assess the effect of ^{39}Ar recoil loss on the dates. Such loss could account for the older dates for the high-temperature steps of the rose mica compared to the green mica. The rose mica step heated as chips yielded younger high-temperature step dates than the one dated using 60/80 mesh material (208 Ma vs. 248 Ma).

The fine-grained green mica 91GS/02-467 yielded an integrated date of 314 Ma. Although Isoplot generated a plateau date for this sample (322 Ma), it is possible that the mica also experienced recoil loss of ^{39}Ar. The last step (1200 °C) yields a date of 224 Ma that approaches the dates of the other mica samples.

An alternative explanation to recoil loss of ^{39}Ar for the range in ages in the mica samples is that mica formed initially during the Carboniferous, corresponding to sparry dolomitisation coinciding with tectonic activity during the Late Devonian–Early Mississip-

pian Antler Orogeny [40]. This mica might then have been partially to wholly reset during the fluid event that formed the Mount Brussilof fersmite.

5.6. Sr Isotopes of Dolomite

The initial Sr isotope ratios range from 0.706115 to 0.728542 (Figure 14). The lower end of this range is similar to seawater at 190 Ma, which was around 0.7075 to 0.7077 [41]. The range to much more radiogenic signatures in the dolomite indicates an older crustal component to the fluids that formed the dolomite. The range in initial Sr isotope values can be explained by deposition of dolomite from hydrothermal fluids that represent variable mixtures of paleo seawater and crustal fluids that have interacted with underlying sedimentary rocks, such as Naiset Formation and Gog Group. Alternatively, the lower Sr isotope values may represent interaction with mantle rocks, which generally (absent significant crustal contamination) have Sr isotope values < 0.706 [42]. Regardless, the range in Sr isotope compositions of dolomite is surprising and suggests multiple stages of growth of dolomite or dynamic fluid mixing conditions.

The Sr isotope data also indicate that the Mount Brussilof system is not a carbonatite or directly related to carbonatitic magmatism. Typical carbonatites have mantle-like Sr isotope compositions (i.e., <0.705; Figure 14), e.g., [43–45].

5.7. Timing of Mount Brussilof Fersmite and Broader Implications of Fersmite Formation

The timing of sparry dolomitisation in the southern Canadian Rocky Mountains remains contentious. There is evidence for at least two periods of sparry dolomitisation coinciding with tectonic activity [46,47]; the first corresponds to the Late Devonian–Early Mississippian Antler Orogeny [40], and the second to the Late Cretaceous–Eocene Laramide Orogeny [48]. A third orogenic phase occurred in the Late Jurassic–Early Cretaceous [49]. Studies by Al-Aasm [47] and Mrad [50] conducted in the northwestern portion of the Western Canada Sedimentary Basin suggest that distinction between different pulses of dolomitisation may be possible based on, for example, $\delta^{18}O$ and $^{87}Sr/^{86}Sr$ values of sparry dolomite and fluid salinity. A comparable study in southeastern British Columbia [51] containing additional information on the solute chemistry of fluid inclusions (Na/Br, Cl/Br, and I/Br values) in dolomite and magnesite suggests that the formation of sparry dolomite, magnesite, talc, and MVT deposits hosted by Middle-Cambrian carbonates preceded the Laramide orogeny. Emerald mineralisation at Mountain River, BC, has a Re–Os isochron age of 345 ± 20 Ma, which has been interpreted to indicate that there was regional fluid flow at this time. This age date is one of the only direct pieces of chronological evidence of Late Devonian–Mississippian regional fluid flow in the Cordillera [52]. These authors suggested that this may support this age for the timing of MVT mineralisation and sparry dolomite formation.

For these reasons, detailed documentation of the Mount Brussilof fersmite occurrence is important, and the timing constraint of fersmite formation will contribute greatly to understanding the metallogeny of southeastern British Columbia. imandl,Petrus [32] documented the relative timing differences between fersmite and magnesite formation; fersmite and sparry dolomite cross-cut magnesite mineralisation, indicating that the ~190 Ma formation of fersmite is a lower age limit for magnesite formation. Therefore, magnesite is either (1) ~coeval but predates fersmite formation, or (2) magnesite formation is significantly older than the fersmite. If the magnesite is approximately coeval with sparry dolomite and fersmite, this would imply that the magnesite is hydrothermal in origin, perhaps related to an evolving fluid resulting from mixing between meteoric and magmatic-hydrothermal fluids carrying Nb and the REE. If, however, the magnesite is significantly older than the

fersmite, this would be consistent with magnesite having a diagenetic origin, as suggested by [2,3].

6. Conclusions

The Mount Brussilof fersmite occurrence is characterised by strongly zoned euhedral crystals growing on the walls of cavities or enclosed in a dolomite matrix. It shares similarities with niobate mineral occurrences reported in 'alpine clefts' and differs texturally from fersmite observed in carbonatite-related Nb mineralisation. The Sr isotope data indicate that the fluids that formed the dolomite were not carbonatitic but variably influenced by Sr derived from crustal sources. Although the Mount Brussilof fersmite occurrence is too small to be of economic interest, our data suggest that at approximately 190 Ma, Nb, and REE were locally transported in fluids along permeable, structurally controlled zones in southeastern British Columbia.

The 190 Ma age estimate on fersmite, in agreement with muscovite dating, provides an approximate upper time constraint on the age of sparry dolomitisation, magnesite ore, and, indirectly, on the emplacement of MVT deposits in the Kicking Horse Rim area of southeastern British Columbia. The scatter in fersmite U-Pb compositions (Figures 11 and 12) probably reflects a degree of disequilibrium, compositional zonation observed in fersmite grains, and either one hydrothermal event of long duration terminating approximately 190 Ma or multiple pulses of hydrothermal activity, with the latest taking place approximately 190 Ma. The variation in our Ar-Ar dates based on relatively disturbed release profiles for micas younger than or of the same age as sparry dolomite is in agreement with this. Additional Ar-Ar dating of mica samples using laser spot dating on larger crystals may cast further light on this.

Supplementary Materials: The following supporting information can be downloaded at https://www.mdpi.com/article/10.3390/min15020128/s1, Figure S1. Backscatter SEM images and false-colour MLA-SEM of sample MB-18A. Figure S2. Backscatter SEM images and false-colour MLA-SEM of sample MB-18B. Figure S3. Backscatter SEM images and false-colour MLA-SEM of sample MB-18C. Figure S4. Regions of interest for data extraction for REE plots in Figure 9. Table S1. MLA-SEM mineralogical results. Table S2. EPMA results for fersmite. Table S3. LA-ICP-MS spot analyses of fersmite. Table S4. U-Pb isotope data. Table S5. 40Ar/39Ar results of mica. Table S6. 87Sr/86Sr results of dolomite intergrown with fersmite.

Author Contributions: Conceptualisation, G.J.S.; methodology, M.I.L., G.J.S., J.A.P., A.V. and A.M.M.; formal analysis, M.I.L., G.J.S., J.A.P. and D.A.; investigation, M.I.L., G.J.S., S.P., J.A.P., A.V. and D.A.; data curation, M.I.L.; writing—original draft preparation, M.I.L., G.J.S. and J.A.P.; writing—review and editing, S.P., C.A., A.V., D.A. and A.M.M.; funding acquisition, G.J.S. All authors have read and agreed to the published version of the manuscript.

Funding: This study is part of the Targeted Geoscience Initiative 5, spearheaded by Natural Resources Canada. Matthew Leybourne acknowledges that this research was undertaken thanks in part to funding from the Canada First Research Excellence Fund through the Arthur B. McDonald Canadian Astroparticle Physics Research Institute.

Data Availability Statement: All data are included with this manuscript.

Acknowledgments: We thank Baymag Inc. for permission to study and sample the Mount Brussilof deposit. Some of the fersmite samples used in this study were provided by Alex Hogg and Brody Myers, mine geologists. The late Mati Raudsepp, Electron-Microbeam/X-Ray Diffraction Facility, Department of Earth, Ocean and Atmospheric Sciences, University of British Columbia, provided the XRD analysis. Earlier versions of this manuscript benefited from improvements and suggestions from Margot McMechan of the Geological Survey of Canada in Calgary.

Conflicts of Interest: The authors declare no conflicts of interest.

References

1. Paradis, S.; Simandl, G.J.; Drage, N.; D'souza, R.; Kontak, D.; Waller, Z. Carbonate-hosted deposits (Mississippi Valley-type, magnesite, and REE-F-Ba) of the southeastern Canadian Cordillera: A review and isotopic data comparison. *Geol. Surv. Can. Bull.* **2022**, *617*, 39–87.
2. Paradis, S.; Simandl, G. *Are There Genetic Links Between Carbonate-Hosted Barite-Zinc-Lead Sulphide Deposits and Magnesite Mineralization in Southeast British Columbia?* Geological Survey of Canada: Ottawa, ON, Canada, 2018; pp. 217–227.
3. Simandl, G.J.; Hancock, K.D. Geology of the Mount Brussilof magnesite deposit, SE British Columbia. In *Geological Fieldwork 1990*; British Columbia Geological Survey: Victoria, BC, Canada, 1991; pp. 269–278.
4. Simandl, G.J.; Hancock, K.D. Sparry Magnesite. In *Geological Fieldwork 1997*; British Columbia Ministry of Employment and Investment: Victoria, BC, Canada, 1998; pp. 24E-1–24E-3.
5. Simandl, G.J.; Hancock, K.D. Sparry Magnesite. In *Selected British Columbia Mineral Deposit Profiles, Industrial Minerals and Gemstones*; Simandl, G.J., Hora, Z.D., Lefebure, D.V., Eds.; British Columbia Ministry of Energy and Mines: Victoria, BC, Canada, 1999; Volume 3, pp. 39–41.
6. Sylvester, P.J.; Jackson, S.E. A Brief History of Laser Ablation Inductively Coupled Plasma Mass Spectrometry (LA–ICP–MS). *Elements* **2016**, *12*, 307–310. [CrossRef]
7. Petrus, J.A.; Chew, D.M.; Leybourne, M.I.; Kamber, B.S. A new approach to laser-ablation inductively-coupled-plasma mass-spectrometry (LA-ICP-MS) using the flexible map interrogation tool 'Monocle'. *Chem. Geol.* **2017**, *463*, 76–93. [CrossRef]
8. Woodhead, J.D.; Hellstrom, J.; Hergt, J.M.; Greig, A.; Maas, R. Isotopic and elemental imaging of geological materials by laser ablation inductively coupled plasma-mass spectrometry. *Geostand. Geoanalytical Res.* **2007**, *31*, 331–353. [CrossRef]
9. Chew, D.M.; Petrus, J.A.; Kamber, B.S. U–Pb LA–ICPMS dating using accessory mineral standards with variable common Pb. *Chem. Geol.* **2014**, *363*, 185–199. [CrossRef]
10. Li, B.; Zhang, W.D.; Zhao, J.X.; Liu, P.; Feng, J.P.; Feng, Y.X.; Xiao, Y. U-Pb geochronology of carbonate-hosted Pb-Zn ores reveals plate-tectonic evolution of eastern Asia during the early Paleozoic. *Sci. Rep.* **2024**, *14*, 25313. [CrossRef]
11. McFarlane, C.R.M. Allanite U Pb geochronology by 193 nm LA ICP-MS using NIST610 glass for external calibration. *Chem. Geol.* **2016**, *438*, 91–102. [CrossRef]
12. Jochum, K.P.; Weis, U.; Stoll, B.; Kuzmin, D.; Yang, Q.; Raczek, I.; Jacob, D.E.; Stracke, A.; Birbaum, K.; Frick, D.A.; et al. Determination of Reference Values for NIST SRM 610-617 Glasses Following ISO Guidelines. *Geostand. Geoanalytical Res.* **2011**, *35*, 397–429. [CrossRef]
13. Aitken, J.D. Birth, growth and death of the Middle Cambrian Cathedral carbonate lithosome, Southern Rocky Mountains. *Bull. Can. Pet. Geol.* **1989**, *37*, 316–333.
14. Aitken, J.D. Control of Lower Paleozoic Sedimentary Facies by the Kicking Horse Rim, Southern Rocky Mountains, Canada. *Bull. Can. Pet. Geol.* **1971**, *19*, 557–569.
15. Aitken, J.D.; Mcllreath, L.A. Comment on "The Burgess Shale: Not in the Shadow of the Cathedral Escarpment". *Geosci. Can.* **1990**, *17*, 111–115.
16. Aitken, J.D.; Mcllreath, L.A. The Cathedral Reef Escarpment, a Cambrian Great Wall with Humble Origins. *Geosci. BC Open File* **1984**, *13*, 17–19.
17. Fritz, W.H. Comment: In Defence of the Escarpment near the Burgess Shale Fossil Locality. *Geosci. Can.* **1990**, *17*, 106–110.
18. Aitken, J.D. Revised models for depositional grand cycles, Cambrian of the southern Rocky Mountains, Canada. *Bull. Can. Pet. Geol.* **1978**, *26*, 515–542.
19. Leech, G.B. *Kananaskis Lakes*; Open File map 634 scale 1:126,720; Geological Survey of Canada: Ottawa, ON, Canada, 1966.
20. McMechan, M.E.; Leech, G.B. *Geology, Mount Assiniboine, British Columbia*; Geological Survey of Canada, Canadian Geoscience Map 13, scale 1:50,000; Natural Resources Canada: Ottawa, ON, Canada, 2011.
21. Layton-Matthews, D.; Hamilton, C.; McClenaghan, M.B. *Modern Techniques and Applications of Mineral Chemistry to Exploration*; Open-File Report; Geological Survey of Canada: Ottawa, ON, Canada, 2017; pp. 10–24.
22. Müller, W.; Shelley, M.; Miller, P.; Broude, S. Initial performance metrics of a new custom-designed ArF excimer LA-ICPMS system coupled to a two-volume laser-ablation cell. *J. Anal. At. Spectrom.* **2009**, *24*, 209–214. [CrossRef]
23. Shi, G.; Li, X.; Li, Q.; Chen, Z.; Deng, J.; Liu, Y.; Kang, Z.; Pang, E.; Xu, Y.; Jia, X. Ion Microprobe U-Pb Age and Zr-in-Rutile Thermometry of Rutiles from the Daixian Rutile Deposit in the Hengshan Mountains, Shanxi Province, China. *Econ. Geol.* **2012**, *107*, 525–535. [CrossRef]
24. Paton, C.; Hellstrom, J.; Paul, B.; Woodhead, J.; Hergt, J. Iolite: Freeware for the visualisation and processing of mass spectrometric data. *J. Anal. At. Spectrom.* **2011**, *26*, 2508. [CrossRef]
25. Petrus, J.A.; Kamber, B.S. VizualAge: A Novel Approach to Laser Ablation ICP-MS U-Pb Geochronology Data Reduction. *Geostand. Geoanalytical Res.* **2012**, *36*, 247–270. [CrossRef]

26. Mayer, C.C.; Jugo, P.J.; Leybourne, M.I.; Grobler, D.F.; Voinot, A. Strontium isotope stratigraphy through the Flatreef PGE-Ni-Cu mineralization at Turfspruit, northern limb of the Bushveld Igneous Complex: Evidence of correlation with the Merensky Unit of the eastern and western limbs. *Min. Depos.* **2021**, *56*, 59–72. [CrossRef] [PubMed]
27. Elburg, M.; Vroon, P.; van der Wagt, B.; Tchalikian, A. Sr and Pb isotopic composition of five USGS glasses (BHVO-2G, BIR-1G, BCR-2G, TB-1G, NKT-1G). *Chem. Geol.* **2005**, *223*, 196–207. [CrossRef]
28. Dalrymple, G.B.; Alexander, E.C.; Lanphere, M.A.; Kraker, G.P. *Irradiation of Samples for 40Ar/39Ar Dating Using the Geological Survey TRIGA Reactor*; U.S. Geological Survey, Professional Paper 1176; U.S. Government Publishing Office: Washington, DC, USA, 1981; p. 55.
29. Steiger, R.H.; Jäger, E. Subcommission Geochronology: Convention on the use of decay constants in geo- and cosmochronology. *Earth Planet. Sci. Lett.* **1977**, *36*, 359–362. [CrossRef]
30. Roddick, J.C. High precision intercalibration of $^{40}Ar/^{39}Ar$ standards. *Geochim. Cosmochim. Acta* **1983**, *47*, 887–898. [CrossRef]
31. Min, K.W.; Mundil, R.; Renne, P.R.; Ludwig, K.R. A test for systematic errors in $^{40}Ar/^{39}Ar$ geochronology through comparison with U/Pb analysis of a 1.1-Ga rhyolite. *Geochim. Cosmochim. Acta* **2000**, *64*, 73–98. [CrossRef]
32. Simandl, G.J.; Petrus, J.A.; Leybourne, M.I.; Paradis, S.; Akam, C. Characterization of primary fersmite from the Mount Brussilof magnesite deposit, southeastern British Columbia, Canada. In *Geological Fieldwork 2018*; British Columbia Geological Survey: Victoria, BC, Canada, 2019; pp. 113–123.
33. Sun, S.-S.; McDonough, W.F. Chemical and isotopic systematics of oceanic basalts: Implications for mantle composition and processes. In *Magmatism in the Ocean Basins*; Saunders, A.D., Norry, M.J., Eds.; Geological Society Special Publications; Geological Society: London, UK, 1989; Volume 42, pp. 313–345.
34. Chakhmouradian, A.R.; Reguir, E.P.; Kressall, R.D.; Crozier, J.; Pisiak, L.K.; Sidhu, R.; Yang, P. Carbonatite-hosted niobium deposit at Aley, northern British Columbia (Canada): Mineralogy, geochemistry and petrogenesis. *Ore Geol. Rev.* **2015**, *64*, 642–666. [CrossRef]
35. Balachandar, S.; Zhang, W.; Liu, Y.; Hu, Z.; Chen, H.; Luo, T.; He, T.; Zeng, X. Bulk analysis of columbite ores by LA-ICP-MS: Development of reference materials and investigation into matrix effects. *J. Anal. At. Spectrom.* **2025**, *40*, 259–275. [CrossRef]
36. Škoda, R.; Novák, M. Y,REE,Nb,Ta,Ti-oxide (AB_2O_6) minerals from REL-REE euxenite-subtype pegmatites of the Třebíč Pluton, Czech Republic; substitutions and fractionation trends. *Lithos* **2007**, *95*, 43–57. [CrossRef]
37. Ercit, T.S. Identification and alteration trends of granitic-pegmatite-hosted (Y,REE,U,Th)-(Nb,Ta,Ti) oxide minerals: A statistical approach. *Can. Mineral.* **1291**, *43*, 1291–1303. [CrossRef]
38. Klemme, S.; Berndt, J. Trace element partitioning between pyrochlore, microlite, fersmite and silicate melts. *Geochem. Trans.* **2020**, *21*, 9. [CrossRef] [PubMed]
39. Roberts, N.M.W.; Drost, K.; Horstwood, M.S.A.; Condon, D.J.; Chew, D.; Drake, H.; Milodowski, A.E.; McLean, N.M.; Smye, A.J.; Walker, R.J.; et al. Laser ablation inductively coupled plasma mass spectrometry (LA-ICP-MS) U–Pb carbonate geochronology: Strategies, progress, and limitations. *Geochronology* **2020**, *2*, 33–61. [CrossRef]
40. Root, K.G. Devonian Antler fold and thrust belt and foreland basin development in the southern Canadian Cordillera: Implication for the Western Canadian Sedimentary Basin. *Bull. Can. Pet. Geol.* **2001**, *49*, 7–36. [CrossRef]
41. McArthur, J.M.; Howarth, R.J.; Bailey, T.R. Strontium isotope stratigraphy: LOWESS Version 3: Best fit to the marine Sr-isotope curve for 0-509 Ma and accompanying look-up table for deriving numerical age. *J. Geol.* **2001**, *109*, 155–170. [CrossRef]
42. White, W.M.; Hofmann, A.W. Sr and Nd isotope geochemistry of oceanic basalts and mantle evolution. *Nature* **1982**, *296*, 821–825. [CrossRef]
43. Amsellem, E.; Schiller, M.; Klausen, M.; Bouyon, A.; Rojas, V.; Bizzarro, M. Origin of carbonatites and associated silicate rocks revealed by Mg triple-isotope approach. *Chem. Geol.* **2023**, *636*, 121663. [CrossRef]
44. Chandra, J.; Upadhyay, D.; Patel, A.K.; Mishra, B. Involvement of syn–, para– and post–magmatic hydrothermal fluids in the alteration of the Kamthai carbonatite complex (India): Insights from in-situ measured 87Sr/86Sr isotope and trace element composition of calcite. *Geochemistry* **2024**, *84*, 126216. [CrossRef]
45. Bell, K.; Simonetti, A. Carbonatite Magmatism and Plume Activity: Implications from the Nd, Pb and Sr Isotope Systematics of Oldoinyo Lengai. *J. Petrol.* **1996**, *37*, 1321–1339. [CrossRef]
46. Al-Aasm, I. Origin and characterization of hydrothermal dolomite in the Western Canadian Sedimentary Basin. *J. Geochem. Explor.* **2003**, *78*, 9–15. [CrossRef]
47. Al-Aasm, I.; Lonnee, J.; Clarke, J. Multiple fluid flow events and the formation of saddle dolomite: Examples from Middle Devonian carbonates of the Western Canada Sedimentary Basin. *J. Geochem. Explor.* **2000**, *69*, 11–15. [CrossRef]
48. Symons, D.T.A.; Enkin, R.J.; Cioppa, M.T. Paleomagnetism in the Western Canada Sedimentary Basin: Dating fluid flow and deformation events. *Bull. Can. Pet. Geol.* **1999**, *47*, 534–547.
49. Vandeginste, V.; Swennen, R.; Gleeson, S.A.; Ellam, R.M.; Osadetz, K.; Roure, F. Geochemical constraints on the origin of the Kicking Horse and Monarch Mississippi Valley-type lead-zinc ore deposits, southeast British Columbia, Canada. *Miner. Depos.* **2007**, *42*, 913–935. [CrossRef]

50. Mrad, C. Fluid Compartmentalization of Devonian and Mississippian Dolostones, Western Canada Sedimentary Basin: Evidence from Fracture Mineralization. Master's Thesis, University of Windsor, Windsor, ON, Canada, 2016.
51. Nesbitt, B.E.; Prochaska, W. Solute chemistry of inclusion fluids from sparry dolomites and magnesites in Middle Cambrian carbonate rocks of the southern Canadian Rocky Mountains. *Can. J. Earth Sci.* **1998**, *35*, 546–555. [CrossRef]
52. Hewton, M.L.; Marshall, D.D.; Ootes, L.; Loughrey, L.E.; Creaser, R.A.; Hanley, J. Colombian-style emerald mineralization in the northern Canadian Cordillera: Integration into a regional Paleozoic fluid flow regime. *Can. J. Earth Sci.* **2013**, *50*, 857–871. [CrossRef]

Disclaimer/Publisher's Note: The statements, opinions and data contained in all publications are solely those of the individual author(s) and contributor(s) and not of MDPI and/or the editor(s). MDPI and/or the editor(s) disclaim responsibility for any injury to people or property resulting from any ideas, methods, instructions or products referred to in the content.